Performance Comparison of Statistical Models for Characterizing Sea Clutter and Ship CFAR Detection in SAR Images

Sheng Gao and Hongli Liu

***Abstract*—A fundamental issue of maritime applications of synthetic aperture radar (SAR) data is the development of precise statistical models for clutter pixels. Several statistical models including the GK, K+R, and $\mathcal{G}_{\mathrm{AO}}$ have been demonstrated to be promising for characterizing sea clutter in SAR images. This article is devoted to investigating the improvements in clutter fitting and ship detection performances by using the recently proposed $\mathcal{G}_{\mathrm{AO}}$, compared to that using the GK and K+R. First, the solution uniqueness of parameter estimators by applying the "method of log cumulants" for the $\mathcal{G}_{\mathrm{AO}}$ is mathematically proven in the first time. Then, we assess the fitting performance of different models for sea surfaces with different wind speed conditions. Next, the constant false alarm rate (CFAR) detection performance of ships based on different models is compared by the indicators of CFAR loss and detection efficiency. Experiments performed on *L*-band ALOS-PALSAR SAR data verify the modeling capability of the $\mathcal{G}_{\mathrm{AO}}$ model for sea clutter. Moreover, several ship detection examples indicate the usefulness and potential of the $\mathcal{G}_{\mathrm{AO}}$ model for CFAR detection in practical applications.**

***Index Terms*—Sea clutter, ship detection, statistical modeling, synthetic aperture radar (SAR).**

I. Introduction

THE ship detection demand for maritime surveillance with high-resolution satellite sensors has increased during the past years [1]. It is of great environmental and economic interest for a variety of military and civilian applications including maritime safety, environmental protection, commercial fishery, and maritime traffic management [2]. Synthetic aperture radar (SAR) is an active imaging system working day and night under all weather conditions and a powerful tool to monitor ships in the open sea and near the coast [3]. Moreover, with the advent of new SAR spaceborne systems, such as RADARSAT-2 [4], TerraSAR-X [5], COSMO-SkyMed [6], ALOS-PALSAR [7], and Sentinel-1 [8], ocean imaging with high resolution and wide coverage can be implemented [9]. As a result, abundant SAR data can be obtained for the ocean; hence, ship detection in spaceborne SAR images is attracting more attention worldwide [1].

Essentially, ship detection in SAR images belongs to a type of anomaly detection that exploits the backscattering responses of SAR differing from the sea background. Literature about ship detection algorithms based on SAR images is abundant. A comprehensive survey of traditional studies of these techniques is given in [2]; more advancements are partially provided in [7]. Among those algorithms, the most widely used technique is the adaptive threshold based on the constant false alarm rate (CFAR) [2], [10], given that ships have a higher radar cross section (RCS) than the surrounding sea background due to metallic materials and corner reflection structures [11]. The pixel amplitudes/intensities of a ship are statistically larger than that of the surrounding sea clutter and can be distinguished based on a reasonable threshold. However, this assumption is not always true in practice; for example, large nonmetallic ships can have a very small radar echo [12]. Several alternative approaches were reported including those based on sublook spectral analyses [13], [14], wavelet transform [15], neural network [16], segmentation [17], nonparametric models [4], [18], [19], feature analysis [20], and convolutional neural network [21]–[24]. In addition, ship detectors based on multi-channel SAR, such as along-track interferometry [25]–[29] and polarimetric analyses [30]–[44], were also proposed, provided that data are available.

This article focuses on ship detection using single-channel/polarization amplitude SAR images. In terms of CFAR ship detection, an accurate description of the sea clutter amplitude probability density function (PDF) is important for robust and reliable CFAR performance. However, modeling sea clutter under different conditions is complex because the radar response of the sea depends on several factors, such as the sea surface characteristics (e.g., sea state, wind speed, and wind direction), imaging geometry (e.g., incidence angle and aspect angle), and radar parameters (e.g., resolution, frequency, polarization, and thermal noise) [45].

Many statistical distributions have been proposed to model the sea clutter in SAR images. Traditionally, the central limit

Manuscript received 25 July 2022; revised 27 August 2022; accepted 29 August 2022. Date of publication 31 August 2022; date of current version 12 September 2022. This work was supported in part by the National Nature Science Foundation of China under Grant 62173133, in part by Nature Science Foundation of Hunan Province under Grant 2020JJ4213, in part by Fundamental Research Funds for the Central Universities under Project 2682020ZT34 and Project 2682021CX071, in part by the CAST Innovation Foundation, and in part by the State Key Laboratory of Geo-Information Engineering under Project SKLGIE2020-Z-3-1 and Project SKLGIE2020-M-4-1. *(Corresponding author: Hongli Liu.)*

Sheng Gao is with the College of Electrical and Information Engineering, Hunan University, Changsha 410082, China, and also with the Inner Mongolia CDC, Huhehot 010000, China (e-mail: gaosh8899@126.com).

Hongli Liu is with the College of Electrical and Information Engineering, Hunan University, Changsha 410082, China (e-mail: honglliu@hnu.edu.cn).

Digital Object Identifier 10.1109/JSTARS.2022.3203230

theorem (CLT) can be exploited when a fully developed speckle regime is achieved and homogeneous surfaces appear as stationary fields. Real and imaginary parts of the received data are therefore assumed to follow a *Gaussian* distribution, which leads to the *Rayleigh* distribution of the single-look amplitude and *Nakagami* distribution (i.e., square root of *gamma*) of the multilook amplitude [48]. These distributions can provide a good fit for SAR sea clutter at low resolution. However, the sea clutter histogram exhibits heavy-tailed characteristics [2], [49] with increasing SAR resolution, which contrasts predictions based on the *Rayleigh* or *Nakagami* distributions.

Several distributions, such as the *log-normal* [50], *Weibull* [51], and *K* models [49], were established to describe heavy-tailed sea clutter. The *Weibull* and *log-normal* distributions are good options to model high-resolution SAR sea clutter in cases in which the *Rayleigh* distribution fails to describe the SAR data, although the *Weibull* and *log-normal* models are empirical/heuristic [52]. The *K* distribution is another model for the characterization of sea clutter and is more popular than the *Weibull* and *log-normal* models. The *K* distribution is based on the well-known compound model [53] in which a fast-varying speckle component is modulated by an uncorrelated and slowly varying texture component (i.e., the underlying RCS component). The speckle part is assumed to be due to the scattering of primarily capillary waves and ripples, while the texture is assumed to originate from ocean gravity waves [54]. Therefore, the *K* distribution is physically based and allows phenomenological interpretation while it considers a nonstationary sea surface (i.e., the corresponding RCS is not a constant). However, as pointed out in [2], the *K* distribution does not always fit the data of sea clutter well, especially in extremely heterogeneous sea regions such as high sea state areas with high wind and wave conditions.

Therefore, several other attempts have been made to replace the *K* distribution when modeling the sea clutter in SAR images. They can be roughly divided into two classes. One option is that the speckle is not fully developed, which makes sense in case of high-resolution cells because the hypothesis satisfying the CLT is no longer valid. Several distribution functions have been established for this class. For example, a *Nakagami-Rice* [55], [56] amplitude distribution may be used when there is one strong reflector in homogeneous clutter. Note that the heavy-tailed Rayleigh distribution [57] and the more recent generalized-K (GK) distribution [58] also belong to this class. The former presents the amplitude distribution by assuming that real and imaginary components follow the zero-mean symmetric *alpha-stable* distribution [59], which can describe impulsive data and has thicker tails than the classical *Rayleigh* distribution. The latter is of interest because it was recently used to describe the statistical behavior of different scattering scenarios in single channel/polarization SAR images; the *K* single-look distribution was considered as a special case [46], [47], [58].

Another way to adapt the *K* distribution is to consider a fully developed speckle hypothesis to be valid and to add more components (e.g., thermal noise and Rayleigh residual). Several useful models, including *K+noise* (K+N) [60], *K+Rayleigh* (K+R) [61], *Pareto+noise* (P+N) [62], *KA* [63], and *KK* [64], [65], have been developed based on the preliminary goal to modify the classical *K* distribution and hence capture sea-spike scattering and thermal noise. Among these models, *KA* and *KK* are difficult to implement in practice because too many parameters need to be estimated [66]. Both the *K* and K+N models are special cases of the K+R model. Moreover, [45] and [66] found that the K+R model can provide a better sea clutter fit than the P+N model. However, it must be noted that only the K+R and P+N models of this distribution class have been recently tested on airborne SAR images [66].

Noticeably, an efficient statistical model, named $\mathcal{G}_{\mathrm{AO}}$, is recently proposed in [67] to flexibly characterize the statistical properties of homogeneous and nonhomogeneous/rough clutter in SAR images. The primary experiments performed on measured SAR data verified the effectiveness of the $\mathcal{G}_{\mathrm{AO}}$ for modeling both SAR land and sea clutter. However, it remains open in the literature and is worth investigating for several issues. On one hand, what is the superiority of the $\mathcal{G}_{\mathrm{AO}}$ in contrast to the other potential models especially in the statistical modeling of SAR sea surface? On the other hand, how well different models perform ship detection in practical applications as a few recently proposed models have not applied to ship detection in SAR images, yet. The motivation of this article is to address the abovementioned issues based on the following fact: the $\mathcal{G}_{\mathrm{AO}}$ model have the same number of parameters [i.e., degree of freedom (DoF)], but a simpler closed-form expression. As a result, it is expected that the $\mathcal{G}_{\mathrm{AO}}$ model is with acceptable or higher fitting accuracy in contrast to popular distributions, and therefore should have good applicability in practice. Moreover, the scope of this article is limited to single-look SAR images because single-look complex (SLC) SAR products are common for current commercial spaceborne SAR satellites (e.g., TerraSAR-X, RADARSAT-2, COSMO-SkyMed, Sentinel-1, and ALOS-PALSAR).

The rest of this article is organized as follows: Several potential models for the characterization of sea clutter in SAR images is presented in Section II. The proof of solution uniqueness of parameter estimators based on the method of log cumulants (MoLC) [68] for the $\mathcal{G}_{\mathrm{AO}}$is provided in Section III. The experimental results are provided in Section IV and the fitting performance of different models for real SAR data is assessed. CFAR performance assessments and several examples of ship detection using different models are also given in this section. Finally, conclusion is listed in Section V.

II. Model Expressions

It is necessary to compare the model with state-of-the-art ones of sea clutter models in the field to verify the effectiveness of the $\mathcal{G}_{\mathrm{AO}}$ model. The compared models are not exhaustive throughout this article. We pay special attention to the comparison with two representative models, including the GK and K+R distributions, because these two models show a high accuracy for real SAR images of sea clutter [46], [58], [66] and the popular and traditional *K* distribution is a special case of GK or K+R distributions. Moreover, in terms of the complexity of the model, GK and K+R are both distributions with three parameters in the case of single look, that is, they have the same DoF as the $\mathcal{G}_{\mathrm{AO}}$ model, which

might be a fair comparison with the $\mathcal{G}_{\text{AO}}$model for fitting actual data.

To fix the notations and terminology, we begin this section by describing the PDFs of the known GK and K+R models. Subsequently, the $\mathcal{G}_{\text{AO}}$ model is provided. For the sake of brevity, only the amplitude versions of the distributions are listed because the transformation from amplitude to intensity PDFs is simple.

A. GK Model

The three-parameter GK distribution has been proposed to characterize the statistics of SLC SAR marine scenes. It is an extension of the well-known single-look *K* distribution used for cases of weak scattering regimes in which a nonuniform distribution of the phase is considered. The amplitude PDF of the GK distribution is given by [58]

$$p_{\text{GK}}(x) = \frac{4\alpha}{\Gamma(\alpha)\eta^{\alpha+1}}\left(\frac{\alpha}{1+\left(\frac{\sigma^2}{4\alpha}\right)}\right)^{\frac{\alpha-1}{2}} x^{\alpha} I_0\left(\frac{\sigma}{\eta}x\right) \times K_{\alpha-1}\left\{\frac{2x}{\eta}\left[\left(1+\frac{\sigma^2}{4\alpha}\right)\alpha\right]^{\frac{1}{2}}\right\},\ \alpha,\eta,\sigma,x>0 \tag{1}$$

where α, η, and σ are the shape, slope, and departure from the uniform distribution of the phase parameters, respectively; $\Gamma(\cdot)$ is the gamma function; $K_{\alpha-1}(\cdot)$ is a modified Bessel function of the second kind with order $\alpha-1$; and $I_0(\cdot)$ is the first kind zero-order modified Bessel function. The parameter estimation method for the GK model was reported in [58].

B. K+R Model

The K+R distribution was recently developed to capture both the thermal noise and additional Rayleigh component [61]. It is also a compound model and uses the following amplitude PDF expression [66]

$$p_{K+R}(x) = \frac{2b^{\nu}x}{\Gamma(\nu)}\int_0^{\infty}\frac{u^{\nu-1}}{u+\tau} \times \exp\left(-\frac{x^2}{u+\tau}-bu\right)du,\ \nu,b,\tau,x>0 \tag{2}$$

where ν is the shape parameter, b is the scale parameter, and $\tau=\tau_n+\tau_r$ indicates the Rayleigh-plus-thermal noise term in which τ_n is the thermal noise component and τ_r is the residual Rayleigh component. As shown in (2), the K+R distribution has also three parameters because $\tau_n+\tau_r$ can be treated as single component in the distribution. Moreover, the K+R distribution has no closed-form expression and numerical integration is required to obtain the solution of the integral. Parameter estimators for the K+R distribution based on the $z\log z$ are given in [60], which reportedly are more efficient than the method-of-moments-based estimators [66].

C. $\mathcal{G}_{AO}$ Model

The PDF of the $\mathcal{G}_{\text{AO}}$ distribution with three parameters for modeling SAR amplitude images of sea clutter is given by [67]

$$p_{\mathcal{G}_{\text{AO}}}(x) = \frac{2^{\mu}\Gamma\left(\mu+\frac{\lambda}{2}\right)}{\beta^{-\lambda}\Gamma(\mu)\Gamma\left(\frac{\lambda}{2}\right)}\frac{x^{\mu-1}\left(\sqrt{\beta^2+x^2}+x\right)^{1-\mu-\lambda}}{\sqrt{\beta^2+x^2}},\quad \mu,\beta,\lambda,x>0 \tag{3}$$

where μ , λ, and β are the model parameters. For the convenience of statements, we hereafter refer to the distribution characterized by (3) as the $\mathcal{G}_{\text{AO}}$ model.

Furthermore, as derived in Appendix A, the mth order moments of the $\mathcal{G}_{\text{AO}}$ model are given by

$$E(x^m) = \left(\frac{\beta}{2}\right)^m \frac{B\left(\frac{\lambda-m}{2},m+\mu\right)}{B\left(\mu,\frac{\lambda}{2}\right)} \tag{4}$$

where $B(\cdot,\cdot)$ is the beta function expressed by $B(a,b)=\frac{\Gamma(a)\Gamma(b)}{\Gamma(a+b)}$ [70].

In practice, the coefficient of variation C_v, defined as the ratio of standard deviation to mean, is generally used as an indicator of homogeneity of the observed scene [48]. That is, the smaller C_v is, the more homogeneous is the observed scene. Based on (4), the relationship between C_v and the $\mathcal{G}_{\text{AO}}$ model parameters can be derived as

$$C_v = \frac{\sqrt{E(x^2)-E^2(x)}}{E(x)} = \sqrt{\frac{B\left(\frac{\lambda-2}{2},2+\mu\right)B\left(\mu,\frac{\lambda}{2}\right)}{B^2\left(\frac{\lambda-1}{2},1+\mu\right)}-1}. \tag{5}$$

As can be seen from (5), C_v is only related to the parameters λ and μ. In other words, the homogeneity of the observed scene can be described by λ and μ. Moreover, under the same homogeneity conditions, that is, fixing the λ and μ, the moments (4) of the $\mathcal{G}_{\text{AO}}$ model are only determined by β. Therefore, we called β, λ, and μ scale, shape, and second shape parameters, respectively.

Fig. 1(a) shows C_v versus λ and μ plot. Based on this figure, C_v seems to exhibit monotonous behavior with respect to λ or μ. However, mathematical proof is not available at present due to the complex deviation of C_v versus λ or μ (5). Fig. 1(b) further compares examples of the $\mathcal{G}_{\text{AO}}$ model with $\beta=1$ for various values of λ and μ, such that the mean is unitary. More heavy-tailed behavior can be obtained for larger C_v values. Moreover, the combination of λ and μ provides more flexibility in controlling the model shape and hence (3) mimics the PDFs with various mode and tail behaviors.

III. Proof of Solution Uniqueness of Parameter Estimation for the $\mathcal{G}_{\text{AO}}$ Model

A crucial step to use the $\mathcal{G}_{\text{AO}}$ model in practical ship detection applications is to estimate the underlying parameters μ, β, and λ based on observed sea clutter data. Nicolas [68] showed that the MoLC is a feasible parametric PDF estimation technique for distributions defined based on $[0,+\infty)$ and an effective tool for the estimation of the parameters of many SAR-specific statistical models [68], [69]. This method estimates the parameters by solving a system of log-cumulant statistics equations.

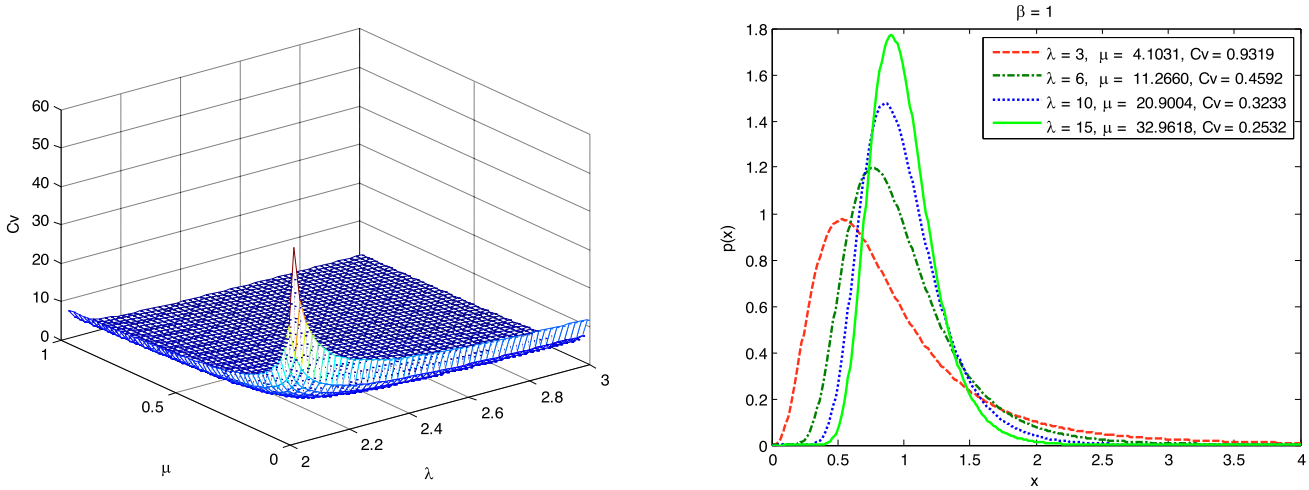

(a) (b)

Fig. 1. (a) Plot of C_v. (b) Plots of several $\mathcal{G}_{\text{AO}}$ PDFs with $\beta = 1$ and unit mean.

A. Parameter Estimators

The log-cumulants of the $\mathcal{G}_{\text{AO}}$ distribution are given by [67]

$$\begin{cases} c_1 = \ln\left(\frac{\beta}{2}\right) - \frac{1}{2}\Psi\left(\frac{\lambda}{2}\right) + \Psi(\mu) - \frac{1}{2}\Psi\left(\frac{\lambda}{2} + \mu\right) \\ c_k = \left(-\frac{1}{2}\right)^k \Psi\left(k-1, \frac{\lambda}{2}\right) + \Psi(k-1, \mu) \\ \qquad -\left(\frac{1}{2}\right)^k \Psi\left(k-1, \frac{\lambda}{2} + \mu\right), \quad k \geq 2 \end{cases} \tag{6}$$

where $\Psi(\cdot)$ represents the digamma function (i.e., the logarithmic derivative of the gamma function) and $\Psi(k, \cdot)$ is the kth order polygamma function (i.e., the kth order derivative of the digamma function).

Based on a sample set $\{x_i\}, i \in [1, N]$, the log-cumulants can be directly acquired using the following relations:

$$\begin{cases} \hat{c}_1 = \dfrac{1}{N}\sum_{i=1}^{N}\left[\ln(x_i)\right] \\ \hat{c}_k = \dfrac{1}{N}\sum_{i=1}^{N}\left[\left(\ln(x_i) - \hat{\hat{c}}_1\right)^k\right], k \geq 2 \end{cases}. \tag{7}$$

Note that the kth log cumulants shown in (6) are independent of the parameter $\beta$when $k \geq 2$. Hence, this allows us to divide the parameter estimates into two stages. First, by combining (6) and (7), the estimates of the underlying parameters μ and λ in the $\mathcal{G}_{\text{AO}}$ model can be obtained based on numerical computation by using the second-order and third-order log-cumulants of $\mathcal{G}_{\text{AO}}$

$$\begin{cases} H\left(\hat{\lambda}, \hat{\mu}\right) = \Psi\left(1, \frac{\hat{\lambda}}{2}\right) + 4\Psi(1, \hat{\mu}) - \Psi\left(1, \frac{\hat{\lambda}}{2} + \hat{\mu}\right) = 4\hat{c}_2 \\ G\left(\hat{\lambda}, \hat{\mu}\right) = -\Psi\left(2, \frac{\hat{\lambda}}{2}\right) + 8\Psi(2, \hat{\mu}) - \Psi\left(2, \frac{\hat{\lambda}}{2} + \hat{\mu}\right) = 8\hat{c}_3 \end{cases} \tag{8}$$

where $\hat{\mu}$ and $\hat{\lambda}$ denote the estimates of the underling parameters μ and λ, respectively. We then insert $\hat{\mu}$ and $\hat{\lambda}$ into the first-order log-cumulants of $\mathcal{G}_{\text{AO}}$. As a result, the estimate $\hat{\beta}$ of the β parameter can be obtained

$$\hat{\beta} = 2\exp\left(\hat{c}_1 + \frac{1}{2}\Psi\left(\frac{\hat{\lambda}}{2}\right) - \Psi(\hat{\mu}) + \frac{1}{2}\Psi\left(\frac{\hat{\lambda}}{2} + \hat{\mu}\right)\right). \tag{9}$$

B. Uniqueness of Solution

As shown in (8) and (9), $\hat{\beta}$ can be obtained after (8) is solved. Therefore, the uniqueness of solution of the parameter estimators only relies on that of (8). In (8), either $H(\hat{\lambda}, \hat{\mu})$ or $G(\hat{\lambda}, \hat{\mu})$ can be regarded as a function of $\hat{\mu}$ and $\hat{\lambda}$. Plots of these two functions with respect to $\hat{\mu}$ and $\hat{\lambda}$ are provided in Fig. 2. Based on Fig. 2, both $H(\hat{\lambda}, \hat{\mu})$ and $G(\hat{\lambda}, \hat{\mu})$ are monotonous functions around $\hat{\mu}$ or $\hat{\lambda}$, which is mathematically proven in Appendix B.

For a certain local scene, $\hat{c}_2$ and $\hat{c}_3$ in (8) are fixed values. In this case, all possible combinations of point $(\hat{\lambda}, \hat{\mu})$ satisfying $H(\hat{\lambda}, \hat{\mu}) = 4\hat{c}_2$ constitute a contour line of Fig. 2(a). Likewise, point $(\hat{\lambda}, \hat{\mu})$ satisfying $G(\hat{\lambda}, \hat{\mu}) = 8\hat{c}_3$ should also be in a contour line of Fig. 2(b). Therefore, the solution of (8) will be the intersection point of the two contour lines.

With respect to the contour line of $H(\hat{\lambda}, \hat{\mu}) = 4\hat{c}_2$, with increasing $\hat{\mu}$, $\hat{\lambda}$ must be decreasing to keep $H(\hat{\lambda}, \hat{\mu})$ a cost $4\hat{c}_2$ because $H(\hat{\lambda}, \hat{\mu})$ is monotonically decreasing with respect to $\hat{\mu}$ or $\hat{\lambda}$, as proven in Appendix B. In other words, $\hat{\lambda}$ should be a curve monotonically decreasing around $\hat{\mu}$ in the contour line of $H(\hat{\lambda}, \hat{\mu}) = 4\hat{c}_2$. With respect to the contour line of $G(\hat{\lambda}, \hat{\mu}) = 8\hat{c}_3$, with increasing $\hat{\mu}$, $\hat{\lambda}$ must be increasing to keep $G(\hat{\lambda}, \hat{\mu})$ a cost $8\hat{c}_3$ because $G(\hat{\lambda}, \hat{\mu})$ is monotonically increasing with respect to $\hat{\mu}$, but monotonically decreasing with respect to $\hat{\lambda}$. This implies that $\hat{\lambda}$ should be a curve monotonically increasing around $\hat{\mu}$ in the contour line of $G(\hat{\lambda}, \hat{\mu}) = 8\hat{c}_3$. Intuitively, two monotonous curves in the $(\hat{\lambda}, \hat{\mu})$ plane should have only one intersection point. That is, the solution of (8) is unique. Fig. 3 shows an example for $H(\hat{\lambda}, \hat{\mu}) = 10$ and $G(\hat{\lambda}, \hat{\mu}) = 1$.

IV. Experiment Analysis

In this section, the $\mathcal{G}_{\text{AO}}$ model is tested on real spaceborne SAR data. The goal is to investigate how the $\mathcal{G}_{\text{AO}}$ model perform in contrast to other models when fitting the histogram of sea clutter data in SAR images. Moreover, the usefulness of the $\mathcal{G}_{\text{AO}}$ model for CFAR ship detection is also investigated.

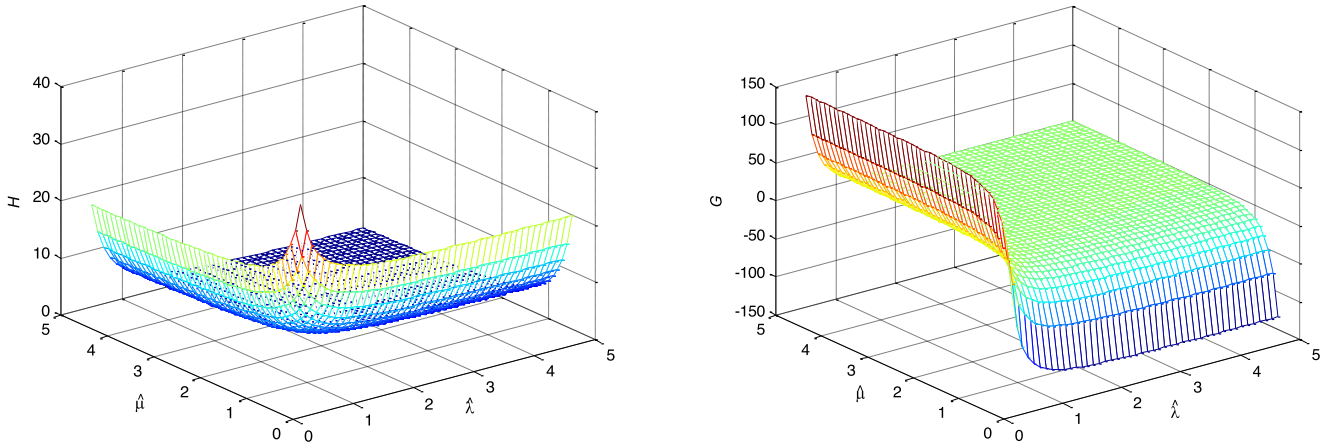

(a) (b)

Fig. 2. Plots of $H(\hat{\lambda}, \hat{\mu})$ and $G(\hat{\lambda}, \hat{\mu})$: (a) $H(\hat{\lambda}, \hat{\mu})$ versus $\hat{\mu}$ and $\hat{\lambda}$. (b) $G(\hat{\lambda}, \hat{\mu})$ versus $\hat{\mu}$ and $\hat{\lambda}$.

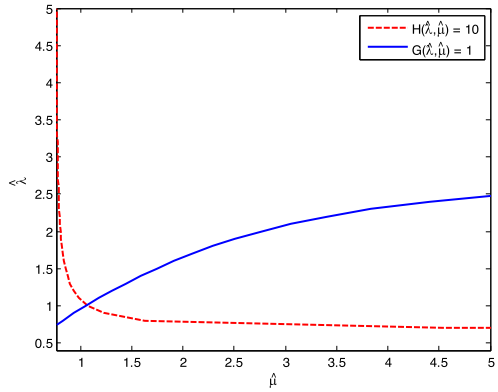

Fig. 3. Curves for $H(\hat{\lambda}, \hat{\mu}) = 10$ and $G(\hat{\lambda}, \hat{\mu}) = 1$.

TABLE I
WIND SPEED INFORMATION

Scene No.	1	2	3	4	5
Wind speed (m/s)	2–4	3–6	9–11	4–7	10–12

A. Test Data

Five large *L*-band level 1.1 ALOS-PALSAR scenes (i.e., scenes 1–5) with different wind conditions were used for the experiments. The data corresponding to these five scenes were collected from June 11 to 19, 2017, in the South China Sea. The slant range resolution is 9.5 m and the azimuth resolution is 4.5 m. The incident angle at the image center was 38.7°. All image products of the scenes are given in SLC format and HH polarization. Because scenes 1–3 contain only pure sea clutter, they were used to test the fitting capability of different distribution models. Scenes 4 and 5 containing ships were used to test the detection performance of different models in practical applications. The wind speed information that corresponds to these five scenes is given in Table I.

B. Comparison of the Fitting Capability

We first examined the effectiveness of the $\mathcal{G}_{\text{AO}}$model. Considering that the sea states of different local sea regions across a large scene might vary [12] and to validate that the statistical model characterized by (3) is appropriate for sea clutter with varying ocean conditions, we divided each scene (see Fig. 4) with a size of 15000 × 4000 pixels in length × width into equally-sized blocks to extract sufficient patch samples of sea clutter regions and sufficient pixel samples for each patch. As a result, each scene was divided into 60 equal blocks. The blocks of scenes 1–3 were numbered patches 1-1–1-60, patches 2-1–2-60, and patches 3-1–3-60 (see Fig. 4), respectively. Therefore, there were a total of 180 patches covering low to high wind speed conditions in this experiment, which allows the determination of the fitting capability of different distributions. All patches have the same size (1000 × 1000 pixels; length × width). Fig. 4 clearly shows that the sea surface of scenes 1–3 is getting rougher (more heterogeneous), because scenes 1–3 correspond to higher and higher wind speed conditions. This is also confirmed by the corresponding C_v values (see Fig. 5).

In this section, we compare the modeling ability of the $\mathcal{G}_{\text{AO}}$ model with that of the GK and K+R distributions. The reason was explained in Section II. In addition, it should be emphasized that the investigation in this subsection supports current research with respect to, at least, two aspects. On one hand, no comparisons between the GK and K+R distributions can be found in the literature, although both models are known to be more advanced than the *K* distribution; on the other hand, the appropriateness of the K+R distribution for measured spaceborne SAR data has not been evaluated, but satellite SAR images may have a low clutter-to-noise ratio.

To reveal the fitting details, the data for each patch were normalized using the mean value. We then applied the PDF defined in (3) to all patches mentioned above. The parameter estimation of the PDF for each patch was accomplished using the parameter estimators based on the MoLC. For comparison, the fitting results of the GK and K+R distributions are also

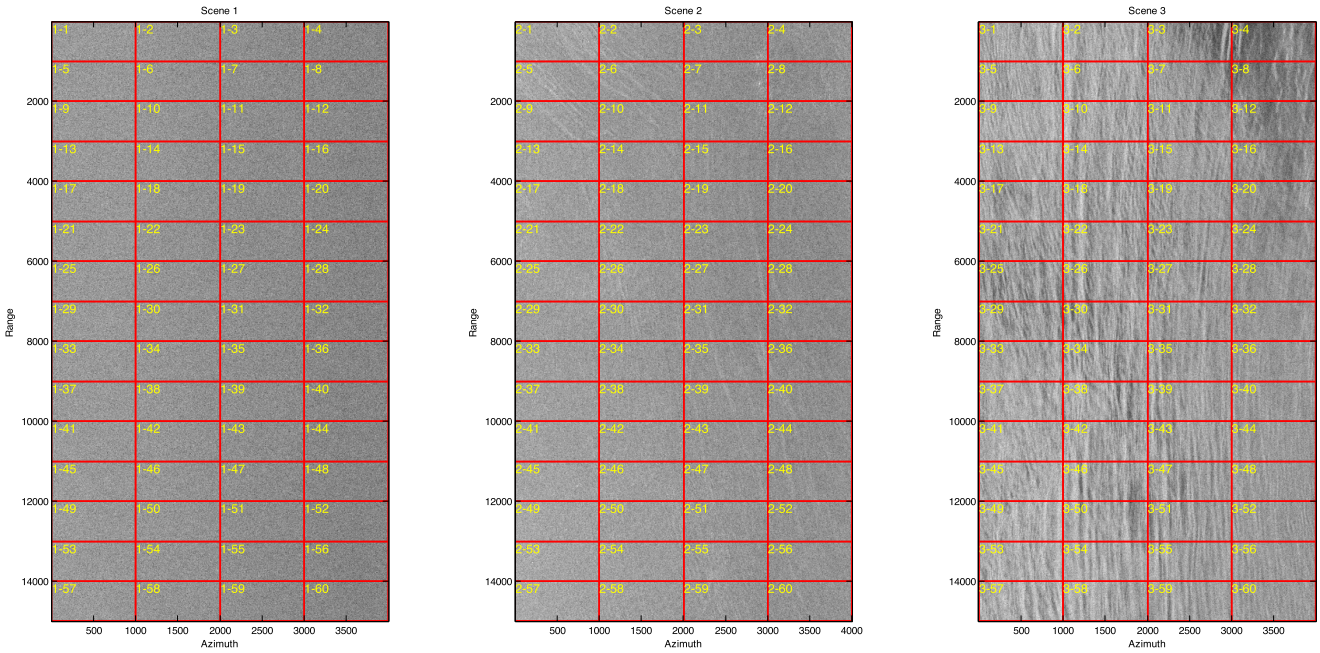

Fig. 4. Several scenes used for the experiments. (a) Scene 1. (b) Scene 2. (c) Scene 3.

TABLE II
QUANTITATIVE COMPARISON OF MEAN FITTING PERFORMANCE BETWEEN DIFFERENT DISTRIBUTIONS

	Mean KL value			Mean TKL value		
	Scene 1	Scene 2	Scene 3	Scene 1	Scene 2	Scene 3
GK	0.0010	0.0013	0.0025	2.1425×10^{-4}	4.0451×10^{-4}	4.2148×10^{-4}
K+R	1.1397×10^{-4}	1.8683×10^{-4}	1.9564×10^{-4}	1.8145×10^{-5}	1.1644×10^{-4}	1.1843×10^{-4}
$\mathcal{G}_{\text{AO}}$	1.1043×10^{-4}	1.7063×10^{-4}	2.1202×10^{-4}	1.7958×10^{-5}	9.7676×10^{-5}	1.3522×10^{-4}

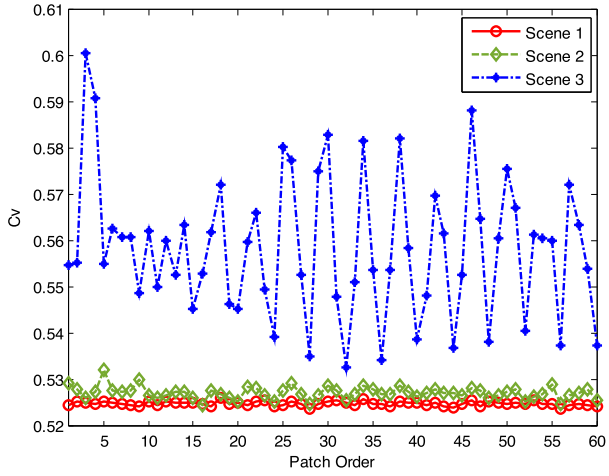

Fig. 5. C_v values of each patch in the three tested scenes.

provided in this section. First, three representative examples were extracted from the tested scenes (for the sake of brevity, the fitting plots of other patches are not shown; instead, the fitting results of all patches are summarized in Tables II and III and Fig. 7). Fig. 6 shows the fitting results for the patches 1–10, 2–34, and 3–4 based on the GK, K+R, and $\mathcal{G}_{\text{AO}}$ models. The fitting results were plotted both on linear and semilog scales to clearly illustrate the details of the results with respect to fitting the whole histogram and tails.

Furthermore, two goodness-of-fit measures were adopted to evaluate the fitting performance for both the overall and tailed parts, that is, to quantitatively compare the fitting accuracy of different distributions in this article. The first measure is the commonly used symmetric Kullback–Leibler (KL) distance [71], which is used to analyze the global similarity between the estimated PDF and data histogram. A small KL value indicates a better entire fit of the particular distribution to real data. The other is the tailed KL (TKL) distance, which quantifies how close an estimated PDF is to the data histogram in the tailed parts. The TKL is a modification focusing on the tail region by computing the KL value between the estimated PDF and data histogram in the range in which the pixel value exceeds a specific threshold because the tail part is the main factor generating false alarms [48]. In this article, the threshold was fixed such that the corresponding probability of false alarm (PFA) of real data [i.e., actual PFA denoted by P_{fa} or, equivalently, the complementary cumulative distribution function (CCDF) value of real data, as employed in [66]] is equal to 10^{-3} for all patches of each scene because a larger actual PFA value is not meaningful for practical target detection [12].

Fig. 7 shows the KL and TKL values of each patch in the three test scenes. It should be noted that the parameters of K+R for

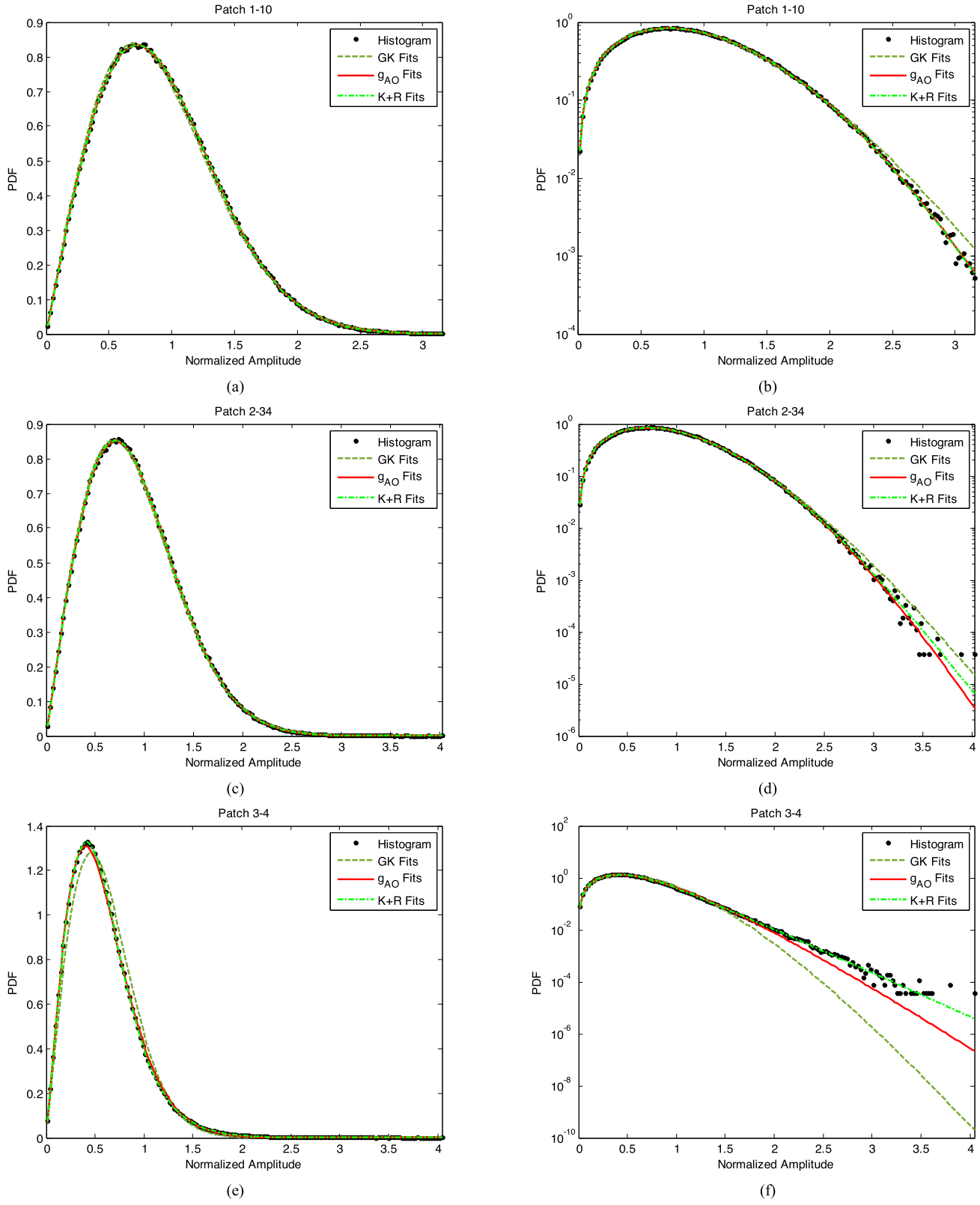

Fig. 6. Fitting results for the three representative patches. (a), (c), and (e) are the fitting results for the amplitude statistics of patches 1–10, 2–34, and 3–4 on a linear scale, respectively. (b), (d), and (f) are the fitting results for the amplitude statistics of patches 1–10, 2–34, and 3–4 on a semilog scale, respectively.

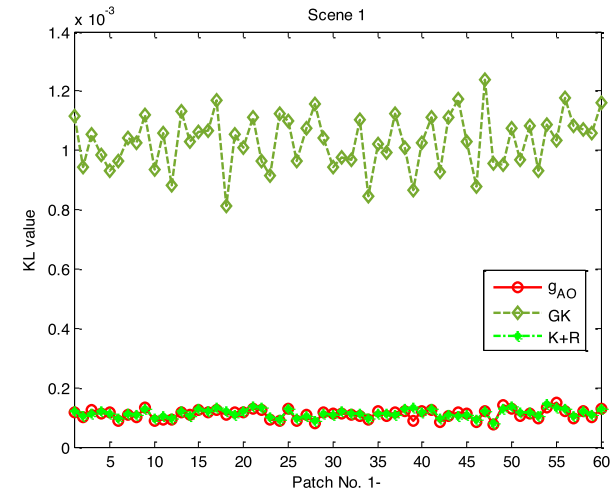

(a)

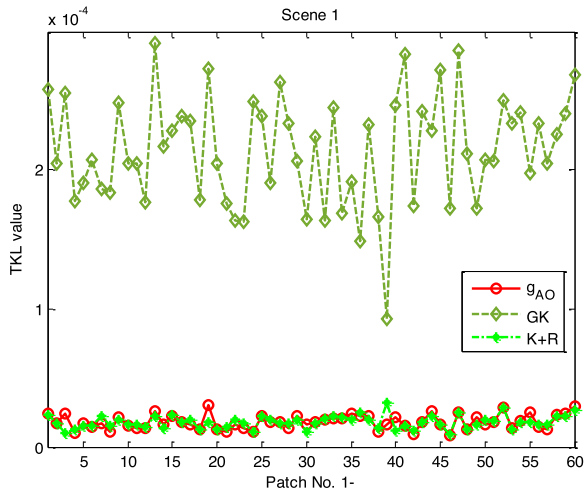

(b)

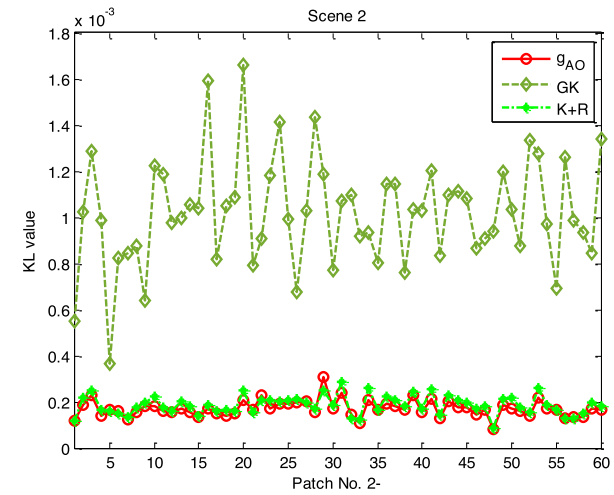

(c)

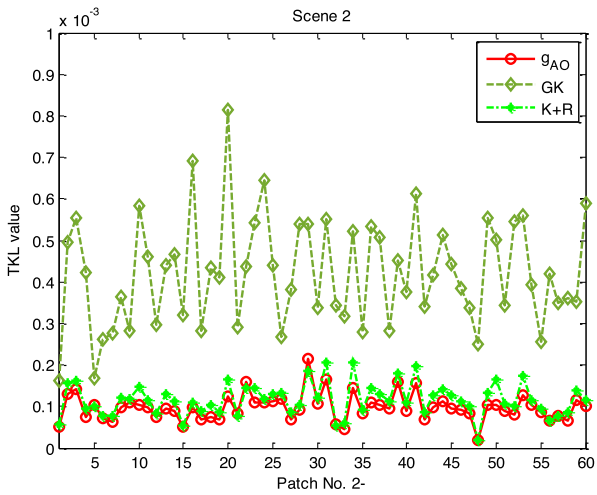

(d)

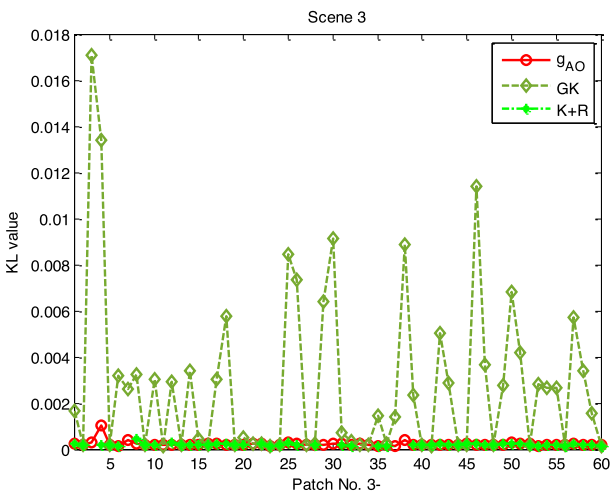

(e)

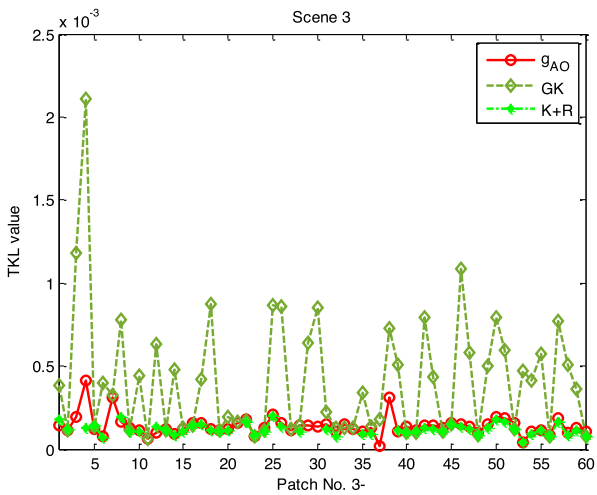

(f)

Fig. 7. Quantitative comparisons of the fitting performance for each patch. (a), (c), and (e) are the KL value of each patch in scenes 1–3, respectively. (b), (d), and (f) are the TKL value of each patch in scenes 1–3, respectively.

TABLE III
COUNT OF PATCHES IN WHICH $\mathcal{G}_{\mathrm{AO}}$ OUTPERFORMS K+R FOR THE THREE SCENES

Scene No.	Number of patches	Number of patches (smaller KL values in $\mathcal{G}_{\mathrm{AO}}$ than in K+R)	Proportion of patches (smaller KL values in $\mathcal{G}_{\mathrm{AO}}$ than in K+R)	Number of patches (smaller TKL values in $\mathcal{G}_{\mathrm{AO}}$ than in K+R)	Proportion of patches (smaller TKL values in $\mathcal{G}_{\mathrm{AO}}$ than in K+R)
1	60	43	71.67%	33	55%
2	60	50	83.33%	55	91.67%
3	49	15	30.61%	9	18.37%

11 patches (patches 3–3, 3–7, 3–11, 3–21, 3–27, 3–29, 3–30, 3–33, 3–34, 3–37, and 3–38) in scene 3 cannot be properly estimated based on $z\log z$-based estimators [66] because the parameter p in the K+R distribution Eq. (2) was always wrongly estimated to be a negative value in these patches. Therefore, the estimated K+R PDFs cannot match the real data histograms. More efficient parameter estimation of the K+R distribution should be investigated in the future; it is beyond the scope of this article. Therefore, hereafter, only the patches with feasible estimated parameters of the K+R distribution in scene 3 are considered. Based on Fig. 7, Table II further presents the mean value of KL and TKL for PDFs considered for each scene.

Based on Figs. 6 and 7 and Table II, it can be observed the following:

1) Regardless of wind speed conditions, both the $\mathcal{G}_{\mathrm{AO}}$ and K+R models provide a better overall fit than the GK distribution. Particularly in regions with higher wind speeds (e.g., the patches in scenes 3), the GK distribution exhibits a large deviation in fitting the overall histogram. This can be clearly seen in Figs. 6(e) and 7(e) and can be confirmed using the resulting mean KL values given in Table II.
2) Similarly, regardless of wind speed conditions, the GK distribution greatly mismatches the tail in most cases of the test patches in the three scenes, while both the $\mathcal{G}_{\mathrm{AO}}$ and K+R models provide a better fit than the GK distribution. This can be seen in both the semilog PDFs shown in Fig. 6(b), (d), and (f) and TKL values depicted in Fig. 7(b), (d), and (f). Overall, a better tail fit performance of the $\mathcal{G}_{\mathrm{AO}}$ or K+R models against the GK model can be obtained on average from Table II.
3) Based on the comparison of the $\mathcal{G}_{\mathrm{AO}}$ and K+R models, the accuracies of entire histogram and tail fits for all patches are rather similar based on the visual inspection of Figs. 6 and 7. Particularly, under low-to-moderate wind speed conditions (i.e., scenes 1 and 2), the $\mathcal{G}_{\mathrm{AO}}$ model on average performs slightly better in fitting the entire histogram and corresponding tailed part than the K+R distribution (see Table II). Table III gives that a higher overall or tail-fitting accuracy is obtained for a large proportion of patches using the $\mathcal{G}_{\mathrm{AO}}$ distribution compared with the K+R model in scenes 1 and 2. However, as opposed to the former situation, the K+R model seems to on average perform slightly better than the $\mathcal{G}_{\mathrm{AO}}$ model under relatively high wind speed conditions (i.e., scene 3) with rougher sea surfaces, regardless if entire histogram or tail fit (see Table II). Moreover, in contrast to the case of relatively homogeneous sea surfaces, the resulting proportion of $\mathcal{G}_{\mathrm{AO}}$ outperforming K+R tends to be smaller in the case of rough sea surfaces of scene 3 (see Table III). The reason might be that the echoes of sea clutter under relatively high wind speed conditions have more severe Rayleigh-plus-thermal noise residues and hence the K+R can better describe them.
4) To summarize, the results indicate that: first, the modeling abilities of the $\mathcal{G}_{\mathrm{AO}}$ and K+R models on average outperform the GK distribution, regardless if overall fit or tail fit and being independent of wind speed conditions; second, the fitting accuracies of the $\mathcal{G}_{\mathrm{AO}}$ and K+R models are similar. From a statistical viewpoint, the K+R model seems to perform slightly better for rough sea surfaces with high wind speed conditions than the $\mathcal{G}_{\mathrm{AO}}$. On the contrary, for relatively homogeneous sea surfaces, the $\mathcal{G}_{\mathrm{AO}}$ is slightly better than the K+R model in terms of fitting accuracy.

TABLE IV
MEAN TIME COMPARISON OF HISTOGRAM FITTING FOR DIFFERENT DISTRIBUTIONS

	Mean time (s)		
	Scene 1	Scene 2	Scene 3
GK	40.0699	40.1029	37.5440
K+R	0.4381	0.4805	0.7303
$\mathcal{G}_{\mathrm{AO}}$	0.4337	0.4311	0.4231

C. Comparison of the Fitting Efficiency

Fig. 8 shows the computation time for histogram fitting of each patch in the three scenes by the three models. Computations were carried out with MATLAB R2014a codes running on an Intel(R) Core(TM) i5-4440 3.1 GHz CPU processor with 8.0 GB memory. Note that the time herein refers to the total time of a complete processing chain including histogram computation, parameter estimation, and model computation. Table IV further provides the mean time of each scene for the foregoing three distributions. The results in Fig. 8 and Table IV indicate that the time cost of histogram fitting is much larger in GK than in both K+R and $\mathcal{G}_{\mathrm{AO}}$ models, mainly due to a time-consuming iterative parameter estimation in GK satisfying the χ^2 hypothesis test [46], [58].

However, the mean computation time for histogram fitting in K+R and $\mathcal{G}_{\mathrm{AO}}$ is in the same order of magnitude, although the latter needs slightly less time. This is because: first, the histogram computation of real data is independent of the distribution models; second, both the parameter estimation based on $z\log z$ in K+R [60] and that based on MoLC in $\mathcal{G}_{\mathrm{AO}}$ involve numerical calculations and have similar computational complexity; and third, the model computation for K+R requires the numerical

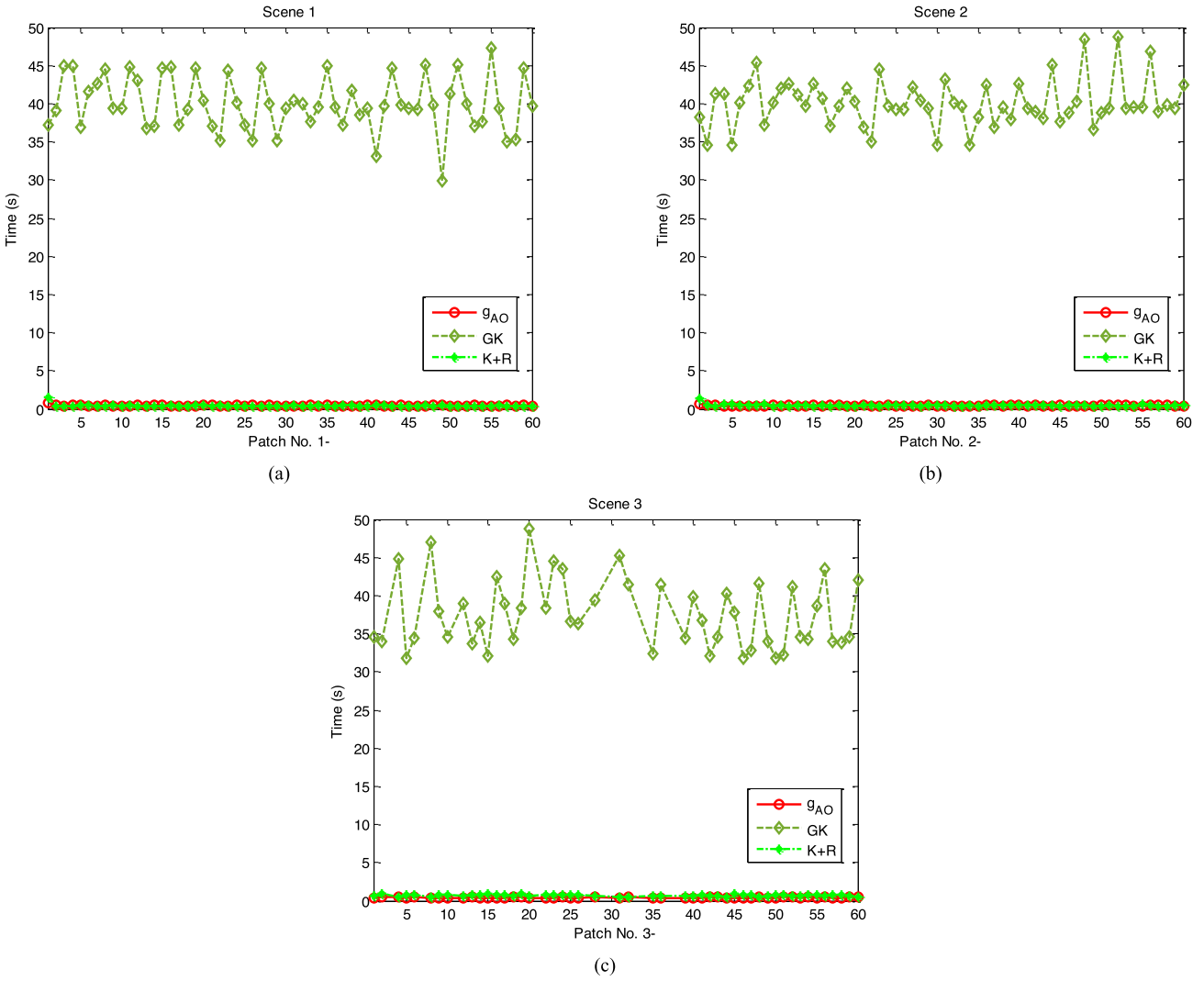

Fig. 8. Computation time of fitting histograms for each patch using the three models. (a)–(c) Correspond to scenes 1–3, respectively.

integral (2). However, the above-mentioned results suggest that the numerical integral is also reliable, stable, and fast.

D. Comparison of the CFAR Detection Performance

After the effectiveness of the $\mathcal{G}_{\mathrm{AO}}$ model in describing actual sea clutter statistics was validated, the next goal was to investigate the performance of the $\mathcal{G}_{\mathrm{AO}}$ model in practical applications of ship CFAR detection to determine how much a better statistical fit to sea clutter improves the ship detection. In the field of CFAR detection, an intuitive understanding for evaluating a better model used for target detection is that the model has a better CFAR maintenance performance (or less CFAR loss) [48]. This CFAR maintenance performance refers to how close the PFA generated by the mode is to the PFA of real data. Therefore, a metric indicating CFAR loss can be defined by

$$C_L(T) = \left| P_{fa}(T) - \hat{P}_{fa}(T) \right| \tag{10}$$

where T is the detection threshold; $P_{fa}(T)$ is the actual PFA of real data under T; and $\hat{P}_{fa}(T)$ is the PFA estimated by the adopted model under T. Clearly, C_L is a function regarding the detection threshold T and indicates the corresponding error between the actual PFA and PFA estimated by the model under any given T.

To avoid possible influences of other factors (e.g., the presence of target pixels) on the assessment of the CFAR maintenance performance, pure clutter data without targets can be used [72]. Therefore, based on the foregoing patches including pure sea clutter in scenes 1–3, we calculated C_L values for each patch for GK, K+R, and $\mathcal{G}_{\mathrm{AO}}$ under $10^{-3} \leq P_{fa} < 10^{-6}$ because a P_{fa} larger than 10^{-3} is not meaningful for target detection and the size of each patch in scenes 1–3 is 10^6 pixels and does not allow a lower P_{fa} value than 10^{-6}. Subsequently, we averaged the C_L results of all patches in each scene for each model to observe the mean CFAR maintenance performance under different wind speed conditions and models. Fig. 9 shows the mean C_L curves plotted against P_{fa}.

From Fig. 9, it can be seen as follows.

1) For all the three scenes, the GK model generates the largest mean CFAR loss. This is reasonable because the GK model exhibits the weakest ability to fit real data, as discussed in Section IV-B.

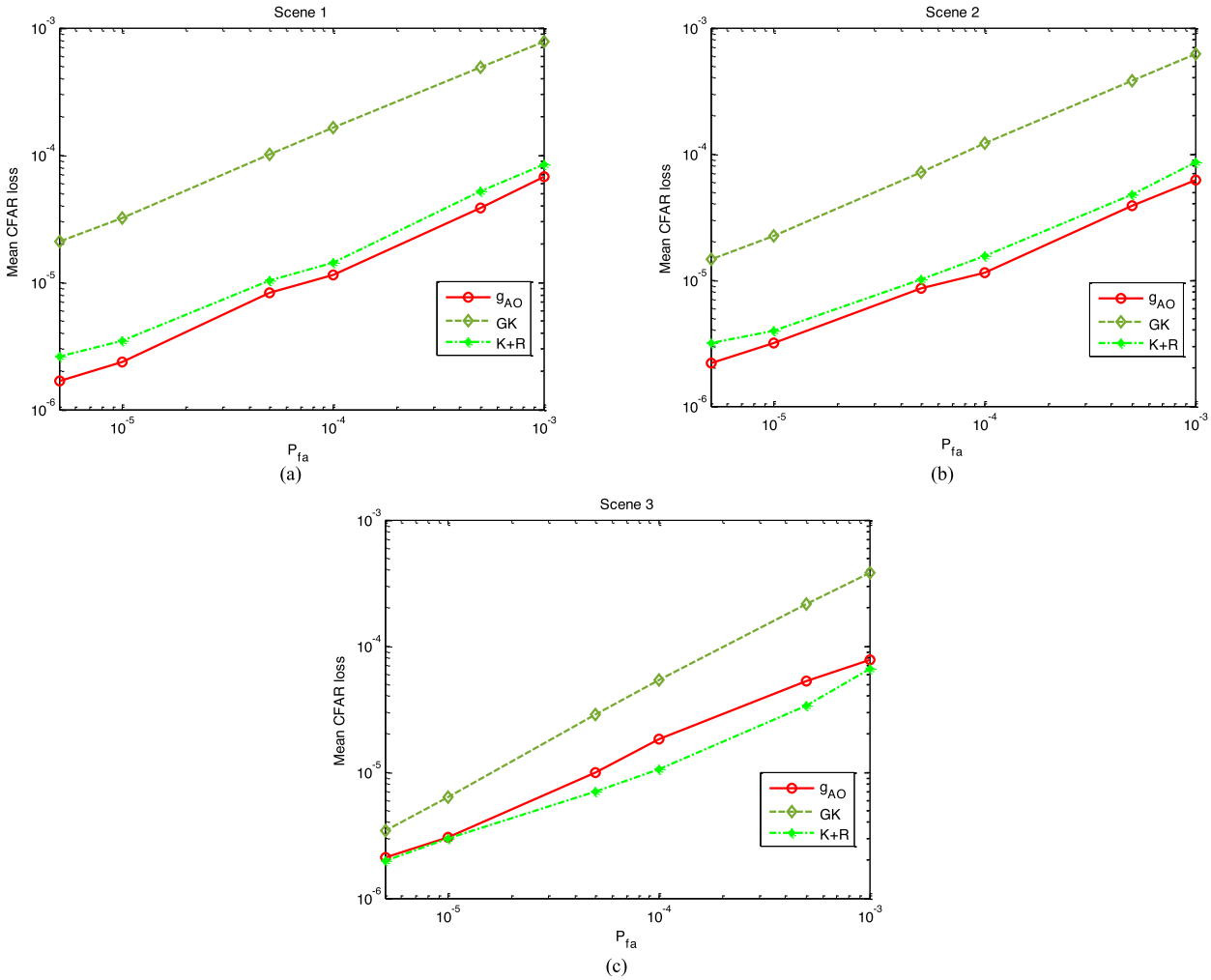

Fig. 9. Comparison of mean CFAR loss for different models. (a) Scene 1. (b) Scene 2. (c) Scene 3.

TABLE V
MEAN CFAR THRESHOLD COMPUTATION TIME FOR DIFFERENT DISTRIBUTIONS

	Mean Time (s)		
	Scene 1	Scene 2	Scene 3
GK	0.0213	0.0211	0.0213
K+R	1.0889	1.0863	1.1328
$\mathcal{G}_{\text{AO}}$	0.0177	0.0208	0.0201

2) In relatively homogeneous sea regions (scenes 1 and 2) with low-to-moderate wind speed conditions, the $\mathcal{G}_{\text{AO}}$ has slightly better CFAR maintenance performance than the K+R model, which is consistent with the result that the $\mathcal{G}_{\text{AO}}$ performs better in fitting the tails of real data in Scenes 1 and 2, as revealed in Section IV-B.
3) On the contrary, in relatively rough sea regions (scene 3) with high wind speed conditions, the CFAR loss of the K+R model is on average slightly better than that of the $\mathcal{G}_{\text{AO}}$ model. This might be due to the fact that the K+R model is particularly useful for rough/heterogeneous sea surfaces (see Section IV-B).
4) In fact, as suggested in Section IV-B, both the K+R and $\mathcal{G}_{\text{AO}}$ models have a very similar fitting accuracy with respect to the three scenes. The CFAR maintenance performance of the two models is also very similar based on the visual inspection of Fig. 9. For example, the difference of the CFAR loss between the two models for $P_{fa} = 10^{-4}$ and scenes 1–3 is 3.0155×10^{-6}, 4.1568×10^{-6}, and 7.5209×10^{-6}, respectively. However, the corresponding difference for $P_{fa} = 10^{-5}$is 1.0915×10^{-6}, 0.7956×10^{-6}, and 0.0852×10^{-6} for the three scenes, respectively. In other words, for the size of 10^6 pixels of each patch in this article, the largest difference of the mean number of false alarms for the two models is on average $\sim$7 pixels for $P_{fa} = 10^{-4}$ and $\sim$1 pixel for $P_{fa} = 10^{-5}$, which shows that the detection performance using K+R and $\mathcal{G}_{\text{AO}}$ is rather similar.

E. Comparison of the Detection Efficiency

The CFAR detection is a complete processing chain including model fitting, CFAR threshold, and two-valued processing comparing each pixel with the threshold. The model fitting efficiency

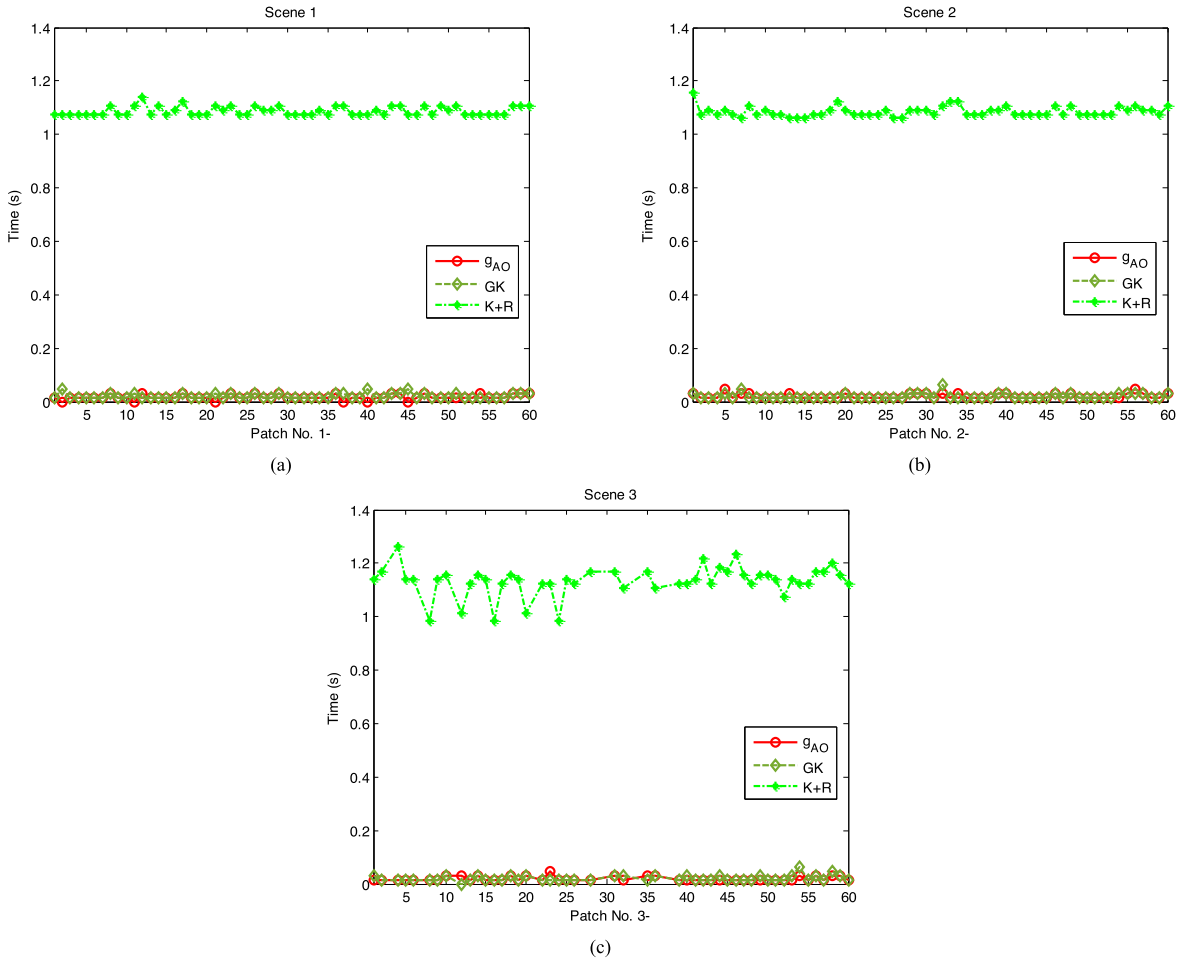

Fig. 10. CFAR threshold computation time for each patch using the three models. (a)–(c) Correspond to scenes 1–3, respectively.

of different models has been analyzed in Section IV-C. For a given patch, the computation time of two-valued processing is the same for any model if only the corresponding CFAR threshold has been obtained. Therefore, the different detection efficiency of various models only relies on the different computation time of the CFAR threshold using these models, except for the different computation time of model fitting. For a model with the PDF expression of $f(x)$, the CFAR threshold T can be obtained by solving the following equation:

$$\bar{P}_{fa} = 1 - \int_0^T f\ x\ dx \tag{11}$$

where $\bar{P}_{fa}$ denotes the theoretical (expected) PFA. In this experiment, we used a preset of $\bar{P}_{fa} = 10^{-4}$. Fig. 10 presents the computation time of the CFAR threshold by solving (11) for each patch using the three models. This figure indicates that the computation time of the CFAR threshold in the GK and $\mathcal{G}_{\text{AO}}$ models is in the same order of magnitude for all patches in the three scenes, but the time consumed by the K+R model is the largest. Table V further provides the mean time of CFAR threshold computation for each scene for different distributions.

As given in Table V, the CFAR threshold computation of GK is slightly more time-consuming than that of $\mathcal{G}_{\text{AO}}$. The reason might be the complex modified Bessel functions of the GK (1). More importantly, because the K+R model cannot be expressed in closed form, an equation involving a dual-integral needs to be solved to acquire a detection threshold for the K+R distribution (2) and (11). This operation solving a dual-integral in K+R is computationally more expensive than that solving a single-integral in either GK or $\mathcal{G}_{\text{AO}}$, as given in Table V.

F. Several Examples of CFAR Detection

The aforementioned analysis only involves pure sea clutter with the absence of ships. In this subsection, we provide some examples including ships to further evaluate how well different models perform ship detection in practical applications; and verify the correctness of the foregoing analysis.

To achieve the abovementioned goals, two examples were used to evaluate the CFAR detection performances utilizing different models. In the first example, a subimage was extracted from scene 4 to investigate the detection ability of different models in the case of a relatively homogeneous sea clutter region, as shown in Fig. 11(a). Five ships, marked as black rectangular boxes, can be observed in this figure. Because of the lack of available automatic identification system data for this region, the ships have to be identified using visual inspection of the enlarged images by trained analysts. In addition, to check the

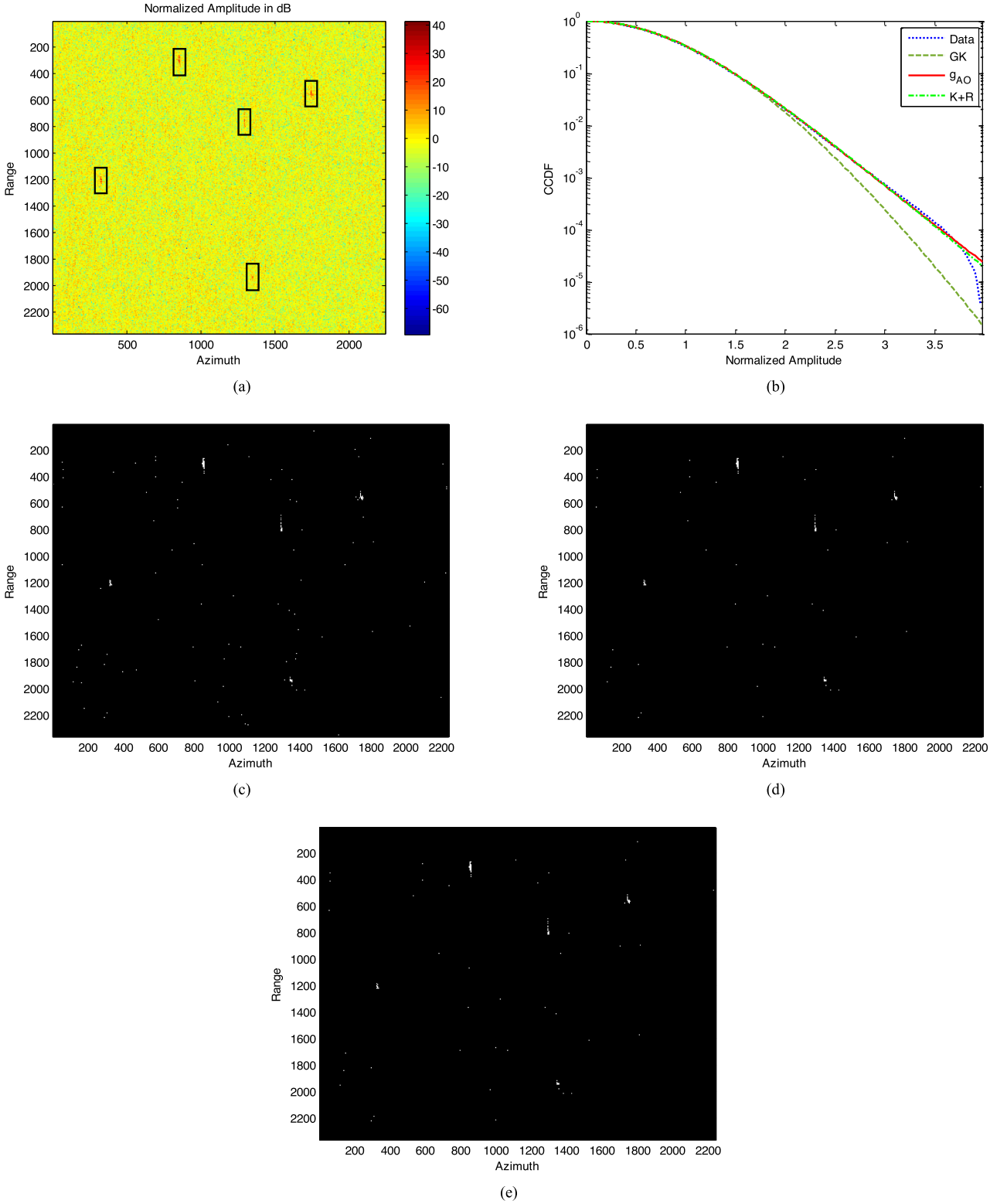

Fig. 11. Detection results for the first example. (a) Normalized amplitude in dB format. (b) CCDF comparisons for different distributions. (c) CFAR detection result of the GK distribution. (d) CFAR detection result of the K+R distribution. (e) CFAR detection result of the $\mathcal{G}_{\mathrm{AO}}$ model.

usefulness of the $\mathcal{G}_{\mathrm{AO}}$ model for ship detection under challenging circumstances of, for example, a high sea state with high wind speeds, the second example was carried out based on a subregion of scene 5 [see Fig. 12(a)], wherein a bright ship is observed based on visual inspection.

Note that the statistical characterization of the tested sea region will be unavoidably affected by the presence of ship pixels. To minimize the impact of man-made structures present in the open sea and avoid corruption of data analysis, a simple filter approach based on the mean and standard deviation of

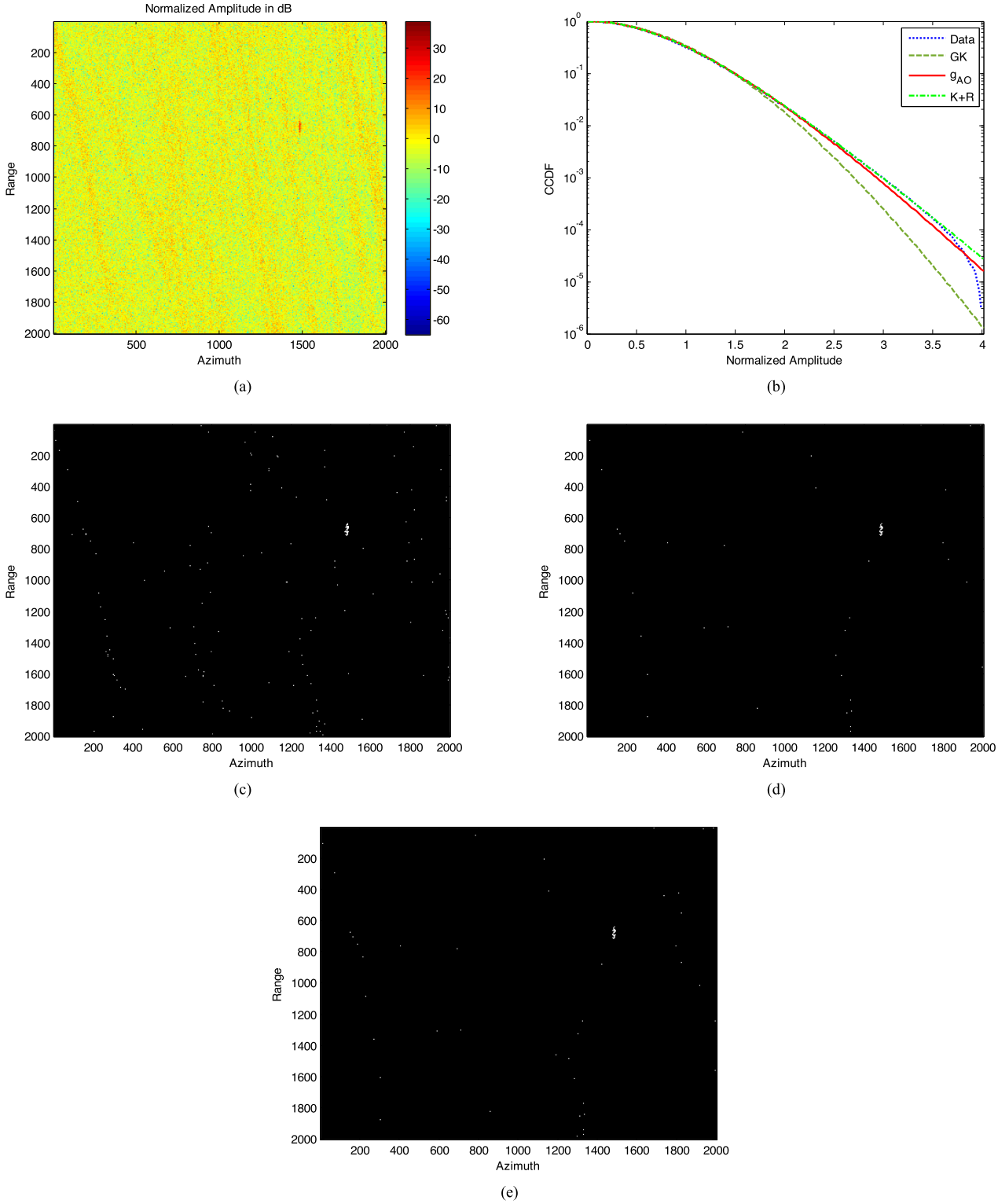

Fig. 12. Detection results for the second example. (a) Normalized amplitude in dB format. (b) CCDF comparisons for different distributions. (c) CFAR detection result of the GK distribution. (d) CFAR detection result of the K+R distribution. (e) CFAR detection result of the $\mathcal{G}_{\mathrm{AO}}$ model.

the region was reported in [73]; see (1) in [73]. After the processing using this approach, potential clutter data were analyzed with the GK, K+R, and $\mathcal{G}_{\mathrm{AO}}$ models. Figs. 11(b) and 12(b) display the CCDF comparisons for different distributions versus the data. Based on these fits and the theoretical false alarm probability $\bar{P}_{fa} = 10^{-4}$, the detection results of the GK, K+R, and $\mathcal{G}_{\mathrm{AO}}$ models are shown in Fig. 11(c)–(e) for the first example and Fig. 12(c)–(e) for the second example, respectively.

Based on Figs. 11 and 12, we can observe the following.

1) Figs. 11(b) and 12(b) show that the GK distribution yields much larger deviations from the tailed part of the

histogram than the $\mathcal{G}_{\text{AO}}$ and K+R models, which implies that the GK distribution has the worst CFAR detection performance. This can be testified based on the comparison of Figs. 11(c) and 12(c) with Figs. 11(d), (e), 12(d), and (e).

2) Based on Figs. 11(b) and 12(b), the K+R and $\mathcal{G}_{\text{AO}}$ models have a rather similar fitting ability for real data. The threshold error between the CCDF of real data and that of the model with fixed $\bar{P}_{fa} = 10^{-4}$ is 0.0399 and 0.0402 for K+R, but 0.0200 and 0.0603 for $\mathcal{G}_{\text{AO}}$ in the two examples, respectively. This suggests that $\mathcal{G}_{\text{AO}}$ is better in the first example but worse in the second example in modeling the real data tails in the case of $\bar{P}_{fa} = 10^{-4}$ compared with K+R. Considering low-to-moderate wind speed conditions in the first example and high wind speed conditions in the second example (see Table I), the results are consistent with those in Section IV-B. However, because the different threshold error between K+R and $\mathcal{G}_{\text{AO}}$ is very small (0.0199 in the first example and 0.0201 in the second example), the CFAR detection performance of the two models should be very similar, as demonstrated in Figs. 11(d), (e), 12(d), and (e).

In addition, the total time (in seconds) of CFAR detection (from data input to detection result output) is 207.9493, 2.4492, and 1.8096 in the first example, and 121.1504, 2.3712, and 1.4820 in the second example for GK, K+R, and $\mathcal{G}_{\text{AO}}$, respectively. The reason was analyzed in Sections IV-C and IV-E. Clearly, GK takes the most time, whilst the K+R model is computationally more expensive than the $\mathcal{G}_{\text{AO}}$ model.

V. Conclusion

Based on the background of ship detection applications utilizing single-channel SAR data, we assessed the fitting performance of the $\mathcal{G}_{\text{AO}}$ model for sea surfaces with different wind speed conditions and compared it with that of several popular models. The preliminary experiments on measured spaceborne SAR data verify the effectiveness of the $\mathcal{G}_{\text{AO}}$ model. Moreover, several ship detection examples demonstrate the usefulness and potential of the $\mathcal{G}_{\text{AO}}$ model for CFAR detection in practical applications.

The main outcomes can be summarized as follows.

1) The GK has the weakest fitting accuracy and highest time cost with respect to ship detection among the three compared models, regardless of wind speed conditions.
2) In terms of the fitting ability, the $\mathcal{G}_{\text{AO}}$ model is slightly better than the K+R model for relatively homogeneous sea clutter with low-to-moderate wind speed conditions. However, the K+R model on average yields a slightly higher fitting accuracy than the $\mathcal{G}_{\text{AO}}$ model in relatively nonhomogeneous sea clutter with high wind speed conditions. Overall, their fitting abilities and CFAR detection performances are very similar.
3) In terms of computation efficiency, the $\mathcal{G}_{\text{AO}}$ model is superior to the K+R model because the CFAR implementation of ship detection of the former is faster than that of the latter because the $\mathcal{G}_{\text{AO}}$ model has the advantage of being expressed in closed form.

Based on the main outcomes mentioned above, the superiority and feasibility using the $\mathcal{G}_{\text{AO}}$ model for ship detection have been verified. More data from various spaceborne SAR sensors will be tested in future. In addition, the generalized Gamma distribution (GΓD) proposed by Li et al. [75] is very popular in the field of statistical modeling of SAR images [76]–[78]. A further comparison between the $\mathcal{G}_{\text{AO}}$ and GΓD for characterizing SAR sea clutter needs also to be deeply investigated in future.

Appendix A
Derivation of mth Order Moments of the $\mathcal{G}_{\text{AO}}$ Distribution

Based on (3), the mth order moments of the $\mathcal{G}_{\text{AO}}$ model can be expressed by

$$E\left(x^m\right) = \int_0^\infty x^m p_{\mathcal{G}_{\text{AO}}}(x)\,dx$$
$$= \frac{2^\mu \Gamma\left(\mu+\frac{\lambda}{2}\right)}{\beta^{-\lambda}\Gamma(\mu)\Gamma\left(\frac{\lambda}{2}\right)} \int_0^\infty \frac{x^{m+\mu-1}\left(\sqrt{\beta^2+x^2}+x\right)^{1-\mu-\lambda}}{\sqrt{\beta^2+x^2}}dx. \tag{A1}$$

According to the integral equation $\int_0^\infty \frac{x^{\mu-1}\left(\sqrt{\beta^2+x^2}+x\right)^\nu}{\sqrt{\beta^2+x^2}}dx = \frac{\beta^{\mu+\nu-1}}{2^\mu}B\left(\mu, \frac{1-\mu-\nu}{2}\right)$ [74], (A1) can be further derived as

$$E\left(x^m\right) = \frac{\beta^m}{2^m}\frac{\Gamma\left(\mu+\frac{\lambda}{2}\right)}{\Gamma(\mu)\Gamma\left(\frac{\lambda}{2}\right)}\frac{\Gamma\left(\frac{\lambda-m}{2}\right)\Gamma(m+\mu)}{\Gamma\left(\frac{\lambda}{2}+\mu+\frac{m}{2}\right)}. \tag{A2}$$

Equation (A2) is completely identical to (4).

Appendix B
Proof That $H(\hat{\lambda},\hat{\mu})$ and $G(\hat{\lambda},\hat{\mu})$ are Monotonous Functions

Let ∂ denote the derivative. Via (11), one can obtain

$$\begin{cases} \frac{\partial H(\hat{\mu},\hat{\lambda})}{\partial\hat{\mu}} = 4\Psi(2,\hat{\mu}) - \Psi\left(2,\frac{\hat{\lambda}}{2}+\hat{\mu}\right) = 3\Psi(2,\hat{\mu}) \\ \qquad\qquad +\Psi(2,\hat{\mu}) - \Psi\left(2,\frac{\hat{\lambda}}{2}+\hat{\mu}\right) \\ \frac{\partial H(\hat{\mu},\hat{\lambda})}{\partial\hat{\lambda}} = \frac{1}{2}\Psi\left(2,\frac{\hat{\lambda}}{2}\right) - \frac{1}{2}\Psi\left(2,\frac{\hat{\lambda}}{2}+\hat{\mu}\right) \end{cases}. \tag{A3}$$

Because $\Psi(2,\cdot)$ is monotonically increasing and negative-valued [70], $\frac{\partial H(\hat{\mu},\hat{\lambda})}{\partial\hat{\mu}} < 0$ and $\frac{\partial H(\hat{\mu},\hat{\lambda})}{\partial\hat{\lambda}} < 0$, which shows that $H(\hat{\lambda},\hat{\mu})$ is monotonically decreasing with respect to $\hat{\mu}$ or $\hat{\lambda}$

$$\begin{cases} \frac{\partial G(\hat{\mu},\hat{\lambda})}{\partial\hat{\mu}} = 8\Psi(3,\hat{\mu}) - \Psi\left(3,\frac{\hat{\lambda}}{2}+\hat{\mu}\right) = 7\Psi(3,\hat{\mu}) \\ \qquad\qquad +\left(\Psi(3,\hat{\mu}) - \Psi\left(3,\frac{\hat{\lambda}}{2}+\hat{\mu}\right)\right) \\ \frac{\partial G(\hat{\mu},\hat{\lambda})}{\partial\hat{\lambda}} = -\frac{1}{2}\Psi\left(3,\frac{\hat{\lambda}}{2}\right) - \frac{1}{2}\Psi\left(3,\frac{\hat{\lambda}}{2}+\hat{\mu}\right) \end{cases}. \tag{A4}$$

As $\Psi(3,\cdot)$ is a strictly monotonically decreasing and positive-valued function [70], $\frac{\partial G(\hat{\mu},\hat{\lambda})}{\partial\hat{\mu}} > 0$ and $\frac{\partial G(\hat{\mu},\hat{\lambda})}{\partial\hat{\lambda}} < 0$. This indicates that $G(\hat{\mu},\hat{\lambda})$ is monotonically increasing with respect to $\hat{\mu}$ but monotonically decreasing with respect to $\hat{\lambda}$.

REFERENCES

[1] K. Ouchi, "Recent trend and advance of synthetic aperture radar with selected topics," *Remote Sens.*, vol. 5, pp. 716–807, Feb. 2013.

[2] D. J. Crisp, "The state-of-the-art in ship detection in synthetic aperture radar imagery," DSTO, Dept. Defence, Australian Government, Canberra, ACT, Australia, Tech. Rep. DSTO-RR-0272, 2004.

[3] S. Brusch, S. Lehner, T. Fritz, M. Soccorsi, A. Soloviev, and B. V. Schie, "Ship surveillance with TerraSAR-X," *IEEE Trans. Geosci. Remote Sens.*, vol. 49, no. 3, pp. 1092–1102, Mar. 2011.

[4] R. Pelich, N. Longepe, G. Mercier, G. Hajduch, and R. Garello, "AIS-based evaluation of target detectors and SAR sensors characteristics for maritime surveillance," *IEEE J. Sel. Topics Appl. Earth Observ. Remote Sens.*, vol. 8, no. 8, pp. 3892–3901, Aug. 2015.

[5] S. Duque, U. Balss, X. Cong, N. Yague-Martinez, and T. Fritz, "Absolute ranging for maritime applications using TerraSAR-X and TanDEM-X data," in *Proc. 10th Eur. Conf. Synthetic Aperture Radar*, 2014, pp. 1405–1408.

[6] F. Nunziata and M. Migliaccio, "On the COSMO-SkyMed pingpong mode to observe metallic targets at sea," *IEEE J. Ocean. Eng.*, vol. 38, no. 1, pp. 71–79, Jan. 2013.

[7] K. Ouchi, "Current status on vessel detection and classification by synthetic aperture radar for maritime security and safety," in *Proc. Symp. Remote Sens. Environ. Sci.*, 2016, pp. 5–12.

[8] R. Torres, P. Snoeij, M. Davidson, D. Bibby, and S. Lokas, "The sentinel-1 mission and its application capabilities," in *Proc. IEEE Int. Geosci. Remote Sens. Symp.*, 2012, pp. 1703–1706.

[9] S. Lehner and B. Tings, "Maritime products using TerraSAR-X and sentinel-1 imagery," in *Proc. Int. Symp. Remote Sens. Environ.*, 2015, pp. 967–973.

[10] K. El-Darymli, P. McGuire, D. Power, and C. Moloney, "Target detection in synthetic aperture radar imagery: A state-of-the-art survey," *J. Appl. Remote Sens.*, vol. 7, pp. 071598–1–071598–35, 2013.

[11] G. Margarit, J. Mallorqui, J. F. Guasch, and C. Lopez-Martinez, "Phenomenological vessel scattering study based on simulated inverse SAR imagery," *IEEE Trans. Geosci. Remote Sens.*, vol. 47, no. 4, pp. 1212–1222, Apr. 2009.

[12] H. Greidanus, M. Alvarez, C. Santamaria, F. Thoorens, N. Kourti, and P. Argentieri, "The SUMO ship detector algorithm for satellite radar images," *Remote Sens*, vol. 9, no. 246, pp. 1–27, 2017.

[13] K. Ouchi, S. Tamaki, H. Yaguchi, and M. Iehara, "Ship detection based on coherence images derived from cross correlation of multilook SAR images," *IEEE Geosci. Remote Sens. Lett.*, vol. 1, no. 3, pp. 184–187, Jul. 2004.

[14] Y. Wang and H. Liu, "A hierarchical ship detection scheme for high-resolution SAR images," *IEEE Trans. Geosci. Remote Sens.*, vol. 50, no. 10, pp. 4173–4184, Oct. 2012.

[15] M. Tello, C. López-Martínez, and J. J. Mallorquí, "A novel algorithm for ship detection in SAR imagery based on the wavelet transform," *IEEE Geosci. Remote Sens. Lett.*, vol. 2, no. 2, pp. 201–205, Feb. 2005.

[16] H. Leung, N. Dubash, and N. Xie, "Detection of small objects in clutter using a GA-RBF neural network," *IEEE Trans. Aerosp. Elect. Syst.*, vol. 38, no. 1, pp. 98–118, Jan. 2002.

[17] P. Lombardo and M. Sciotti, "Segmentation-based technique for ship detection in SAR images," *IEE Proc. Radar, Sonar Navig.*, vol. 148, no. 3, pp. 147–159, Jun. 2001.

[18] G. Gao, "A Parzen-window-kernel-based CFAR algorithm for ship detection in SAR images," *IEEE Geosci. Remote Sens. Lett.*, vol. 8, no. 3, pp. 557–561, May 2011.

[19] Y. Cui, "On semiparametric clutter estimation for ship detection in synthetic aperture radar images," *IEEE Trans. Geosci. Remote Sens.*, vol. 51, no. 5, pp. 3170–3180, May 2013.

[20] C. Wang, S. Jiang, H. Zhang, F. Wu, and B. Zhang, "Ship detection for high-resolution SAR images based on feature analysis," *IEEE Geosci. Remote Sens. Lett.*, vol. 11, no. 1, pp. 119–123, Jan. 2014.

[21] Z. Cui, Q. Li, Z. Cao, and N. Liu, "Dense attention pyramid networks for multi-scale ship detection in SAR images," *IEEE Trans. Geosci. Remote Sens.*, vol. 57, no. 11, pp. 8983–8997, Nov. 2019.

[22] S. Ren, K. He, R. Girshick, and J. Sun, "Faster R-CNN: Towards real time object detection with region proposal networks," *IEEE Trans. Pattern Anal. Mach. Intell.*, vol. 39, no. 6, pp. 1137–1149, Jun. 2017.

[23] L. Zhou, H. Yu, Y. Lan, S. Gong, and M. Xing, "Canet: An unsupervised deep convolutional neural network for efficient cluster-analysis-based multibaseline INSAR phase unwrapping," *IEEE Trans. Geosci. Remote Sens.*, vol. 60, pp. 1–15, 2021.

[24] Q. Fan et al., "Ship detection using a fully convolutional network with compact polarimetric SAR images," *Remote Sens.*, vol. 11, no. 18, 2019, Art. no. 2171.

[25] E. Makhoul, A. Broquetas, J. R. Rodon, Y. Zhan, and F. Ceba, "A performance evaluation of SAR-GMTI missions for maritime applications," *IEEE Trans. Geosci. Remote Sens.*, vol. 53, no. 5, pp. 2496–2509, May 2015.

[26] G. Gao, X. Wang, and T. Lai, "Detection of moving ships based on a combination of magnitude and phase in along-track interferometric SAR – part I: SIMP metric and its performance," *IEEE Trans. Geosci. Remote Sens.*, vol. 53, no. 7, pp. 3565–3581, Jul. 2015.

[27] G. Gao, X. Wang, and T. Lai, "Detection of moving ships based on a combination of magnitude and phase in along-track interferometric SAR – part II: Statistical modeling and CFAR detection," *IEEE Trans. Geosci. Remote Sens.*, vol. 53, no. 7, pp. 3582–3599, Jul. 2015.

[28] G. Gao and G. Shi, "The CFAR detection of ground moving targets based on a joint metric of SAR interferogram's magnitude and phase," *IEEE Trans. Geosci. Remote Sens.*, vol. 50, no. 9, pp. 3618–3624, Sep. 2012.

[29] G. Gao and G. Shi, "Ship detection in dual-channel ATI-SAR based on the notch filter," *IEEE Trans. Geosci. Remote Sens.*, vol. 55, no. 8, pp. 4795–4810, Aug. 2017.

[30] C. Liu, P. W. Vachon, and G. W. Geling, "Improved ship detection with airborne polarimetric SAR data," *Can. J. Remote Sen.*, vol. 31, pp. 122–131, 2005.

[31] A. Marino, "A notch filter for ship detection with polarimetric SAR data," *IEEE J. Sel. Topics Appl. Earth Observ. Remote Sens.*, vol. 6, no. 3, pp. 1219–1232, Jun. 2013.

[32] G. Gao and G. Shi, "CFAR ship detection in nonhomogeneous sea clutter using polarimetric SAR data based on the notch filter," *IEEE Trans. Geosci. Remote Sens.*, vol. 55, no. 8, pp. 4811–4824, Aug. 2017.

[33] G. Gao, S. Gao, J. He, and G. Li, "Adaptive ship detection in hybrid-polarimetric SAR images based on the power-entropy decomposition," *IEEE Trans. Geosci. Remote Sens.*, vol. 56, no. 9, pp. 5394–5407, Sep. 2018.

[34] G. Gao, S. Gao, J. He, and G. Li, "Ship detection using compact polarimetric SAR based on the notch filter," *IEEE Trans. Geosci. Remote Sens.*, vol. 56, no. 9, pp. 5380–5393, Sep. 2018.

[35] R. Shirvany, M. Chabert, and J. Y. Tourneret, "Ship and oil-spill detection using the degree of polarization in linear and hybrid/compact dual-pol SAR," *IEEE J. Sel. Topics Appl. Earth Observ. Remote Sens.*, vol. 5, no. 3, pp. 885–892, Jun. 2012.

[36] F. Nunzaita, M. Migliaccio, and C. E. Brown, "Reflection symmetry for polarimetric observation of man-made metallic targets at sea," *IEEE J. Ocean. Eng.*, vol. 37, no. 3, pp. 384–394, Jul. 2012.

[37] T. Liu, J. Zhang, G. Gao, J. Yang, and A. Marino, "CFAR ship detection in polarimetric synthetic aperture radar images based on whitening filter," *IEEE Trans. Geosci. Remote Sens.*, vol. 58, no. 1, pp. 58–81, Jan. 2020.

[38] T. Liu, Z. Yang, A. Marino, G. Gao, and J. Yang, "Robust CFAR detector based on truncated statistics for polarimetric synthetic aperture radar," *IEEE Trans. Geosci. Remote Sens.*, vol. 58, no. 9, pp. 6731–6747, Sep. 2020.

[39] T. Liu, Z. Yang, A. Marino, G. Gao, and J. Yang, "PolSAR ship detection based on neighborhood polarimetric covariance matrix," *IEEE Trans. Geosci. Remote Sens.*, vol. 59, no. 6, pp. 4874–4887, Jun. 2021.

[40] L. Zhang, G. Gao, C. Chen, S. Gao, and L. Yao, "Compact polarimetric synthetic aperture radar for target detection: A review," *IEEE Geosci. Remote Sens. Mag.*, early access, doi: 10.1109/MGRS.2022.3186904.

[41] T. Liu, Y. Jiang, A. Marino, G. Gao, and J. Yang, "The polarimetric detection optimization filter and its statistical test for ship detection," *IEEE Trans. Geosci. Remote Sens.*, vol. 60, 2022, Art. no. 5202218.

[42] T. Liu, Z. Yang, A. Marino, G. Gao, and J. Yang, "Joint polarimetric subspace detector based on modified linear discriminant analysis," *IEEE Trans. Geosci. Remote Sens.*, vol. 60, 2022, Art. no. 5223519, doi: 10.1109/TGRS.2022.3148979.

[43] R. Touzi, J. Hurley, and P. W. Vachon, "Optimization of the degree of polarization for enhanced ship detection using polarimetric RADARSAT-2," *IEEE Trans. Geosci. Remote Sens.*, vol. 53, no. 10, pp. 5403–5424, Oct. 2015.

[44] G. Gao, Y. Luo, K. Ouyang, and S. Zhou, "Statistical modeling of PMA detector for ship detection in high-resolution dual-polarization SAR images," *IEEE Trans. Geosci. Remote Sens.*, vol. 54, no. 7, pp. 4302–4313, Jul. 2016.

[45] A. Fiche, S. Angelliaume, L. Rosenberg, and A. Khenchaf, "Statistical analysis of low grazing angle high resolution X-band SAR sea clutter," in *Proc. IEEE Int. Radar Conf.*, 2014, pp. 1–6.
[46] G. Ferrara, M. Migliaccio, F. Nunziata, and A. Sorrentino, "GK-based observation of metallic targets at sea in full-resolution SAR data: A multipolarization study," *IEEE J. Ocean. Eng.*, vol. 36, no. 2, pp. 195–204, May 2011.
[47] D. Velotto, M. Soccorsi, and S. Lehner, "Azimuth ambiguities removal for ship detection using full polarimetric X-band SAR data," *IEEE Trans. Geosci. Remote Sens.*, vol. 52, no. 1, pp. 76–88, Jan. 2014.
[48] C. J. Oliver and S. Quegan, *Understanding Synthetic Aperture Radar Images*. Norwood, MA, USA: Artech House, 1998.
[49] E. Jakeman and P. N. Pusey, "A model for non-Rayleigh sea echo," *IEEE Trans. Antennas Propag.*, vol. 24, pp. 806–814, 1976.
[50] G. Goldstein, "False-alarm regulation in log-normal and weibull clutter," *IEEE Trans. Aerosp. Electron. Syst.*, vol. AES-9, no. 1, pp. 84–92, Jan. 1973.
[51] G. V. Trunk and S. F. George, "Detection of targets in non-Gaussian sea clutter," *IEEE Trans. Aerosp. Electron. Syst.*, vol. AES-6, no. 5, pp. 620–628, Sep. 1970.
[52] M. Messina, M. Greco, and G. Pinelli, "Statistical characterization of high resolution SAR images under different sea state conditions," in *Proc. IEEE Gold Remote Sens. Conf.*, 2010, pp. 1–3.
[53] K. D. Ward, "Compound representation of high resolution sea clutter," *Electron. Lett.*, vol. 17, no. 16, pp. 561–563, Aug. 1981.
[54] M. Farshchian and F. L. Posner, "The pareto distribution for low grazing angle and high resolution X-band sea clutter," in *Proc. IEEE Radar Conf.*, 2010, pp. 789–793.
[55] R. Dana and D. Knepp, "The impact of strong scintillation on space based radar design II: Noncoherent detection," *IEEE Trans. Aerosp. Electron. Syst.*, vol. AES-22, no. 1, pp. 34–36, Jan. 1986.
[56] C. Tison, J. M. Nicolas, F. Tupin, and H. Maitre, "A new statistical model for Markovian classification of urban areas in high-resolution SAR images," *IEEE Trans. Geosci. Remote Sens.*, vol. 42, no. 10, pp. 2046–2057, Oct. 2004.
[57] E. E. Kuruoglu and J. Zerubia, "Modeling SAR images with a generalization of the Rayleigh distribution," *IEEE Trans. Image Process.*, vol. 13, no. 4, pp. 527–533, Apr. 2004.
[58] M. Migliaccio, G. Ferrara, A. Gambardella, F. Nunziata, and A. Sorrentino, "A physically consistent speckle model for marine SLC SAR images," *IEEE J. Ocean. Eng.*, vol. 32, no. 4, pp. 839–847, Oct. 2007.
[59] M. Liao, C. Wang, Y. Wang, and L. Jiang, "Using SAR images to detect ships from sea clutter," *IEEE Geosci. Remote Sens. Lett.*, vol. 5, no. 2, pp. 194–198, Apr. 2008.
[60] M. Sahed, A. Mezache, and T. Laroussi, "A novel [zlogz]-based closed form approach to parameter estimation of K-distributed clutter plus noise for radar detection," *IEEE Trans. Aerosp. Electron. Syst.*, vol. 51, no. 1, pp. 492–505, Jan. 2015.
[61] L. Rosenberg, S. Watts, and S. Bocquet, "Application of the K+Rayleigh distribution to high grazing angle sea-clutter," in *Proc. IEEE Int. Radar Conf.*, 2014, pp. 1–6.
[62] L. Rosenberg and S. Bocquet, "Application of the pareto plus noise distribution to medium grazing angle sea-clutter," *IEEE J. Sel. Topics Appl. Earth Observ. Remote Sens.*, vol. 8, no. 1, pp. 255–261, Jan. 2015.
[63] D. Middleton, "New physical-statistical methods and models for clutter and reverberation: The KA distribution and related probability structures," *IEEE J. Ocean. Eng.*, vol. 24, no. 3, pp. 261–284, Jul. 1999.
[64] Y. Dong, "Distribution of X-band high resolution and high grazing angle sea clutter," Def. Sci. Technol. Org., Canberra, ACT, Australia, Tech. Rep. DSTO-RR-0316, 2006.
[65] L. Rosenberg, D. J. Crisp, and N. J. Stacy, "Analysis of the KK-distribution with medium grazing angle sea-clutter," *IET Radar Sonar Navigat.*, vol. 4, no. 2. pp. 209–222, Apr. 2010.
[66] A. Fiche, S. Angelliaume, L. Rosenberg, and A. Khenchaf, "Analysis of X-band SAR sea-clutter distributions at different grazing angles," *IEEE Trans. Geosci. Remote Sens.*, vol. 53, no. 8, pp. 4650–4660, Aug. 2015.
[67] G. Gao, S. Gao, K. Ouyang, J. He, and G. Li, "Scheme for characterizing clutter statistics in SAR amplitude images by combining two parametric models," *IEEE Trans. Geosci. Remote Sens.*, vol. 56, no. 10, pp. 5636–5646, Oct. 2018.
[68] J. M. Nicolas, "Introduction to second kind statistic: Application of log-moments and log-cumulants to SAR image law analysis," *Traitement du Signal*, vol. 19, no. 3, pp. 139–167, 2002.
[69] V. A. Krylov, G. Moser, S. B. Serpico, and J. Zerubia, "On the method of logarithmic cumulants for parametric probability density function estimation," *IEEE Trans. Image Process.*, vol. 22, no. 10, pp. 3791–3806, Oct. 2013.
[70] M. Abramowitz and I. A. Stegun, *Handbook of Mathematical Functions*. New York, NY, USA: Dover, 1972.
[71] S. Kullback and R. A. Leibler, "On information and sufficiency," *Ann. Math. Statist.*, vol. 22, no. 1, pp. 79–86, Mar. 1951.
[72] X. Qin, S. Zhou, H. Zou, and G. Gao, "A CFAR detection algorithm for generalized gamma distributed background in high-resolution SAR images," *IEEE Geosci. Remote Sens. Lett.*, vol. 10, no. 4, pp. 806–810, Jul. 2013.
[73] E. Makhoul, C. Lopez-Martinez, and A. Broquetas, "Exploiting polarimetric TerraSAR-X data for sea clutter characterization," *IEEE Trans. Geosci. Remote Sens.*, vol. 54, no. 1, pp. 358–372, Jan. 2016.
[74] S. I. Gradshteyn and I. M. Ryzhik, *Table of Integrals, Series, and Products*. San Diego, CA, USA: Academic, 2007.
[75] H. C. Li, W. Hong, Y. R. Wu, and P. Z. Fan, "On the empirical-statistical modeling of SAR images with generalized gamma distribution," *IEEE J. Sel. Top. Signal Process.*, vol. 5, no. 3, pp. 386–397, Jun. 2011.
[76] H. C. Li, V. A. Krylov, P. Z. Fan, J. Zerubia, and W. J. Emery, "Unsupervised learning of generalized gamma mixture model with application in statistical modeling of high-resolution SAR images," *IEEE Trans. Geosci. Remote Sens.*, vol. 54, no. 4, pp. 2153–2170, Apr. 2016.
[77] G. Gao, K. Ouyang, Y. Luo, S. Liang, and S. Zhou, "Scheme of parameter estimation for generalized gamma distribution and its application to ship detection in SAR images," *IEEE Trans. Geosci. Remote Sens.*, vol. 55, no. 3, pp. 1812–1832, Mar. 2017.
[78] V. A. Krylov, G. Moser, S. B. Serpico, and J. Zerubia, "On the method of logarithmic cumulants for parametric probability density function estimation," *IEEE Trans. Image Process.*, vol. 22, no. 10, pp. 3791–3806, Oct. 2013.

Sheng Gao was born in Inner Mongolia Province, China, in 1979. He received the B.S. and M.S. degrees from the Inner Mongolia University of Science and Technology, Baotou, China, in 2002 and 2013, respectively. He is currently working on SAR target detection toward the Ph.D. degree in energy and environment.

His current research interests include image processing and pattern recognition.

Hongli Liu received the B.Sc. degree in electrical engineering and the Ph.D. degree in control theory and engineering from Hunan University, Changsha, China, in 1985 and 2000, respectively.

He is currently a Professor with the College of Electrical and Information Engineering, Hunan University. His current research interests include intelligent information processing and transmission technology.